

# Giant Tunable Mechanical Nonlinearity in Graphene-Silicon Nitride Hybrid Resonator

Rajan Singh,<sup>1</sup> Arnab Sarkar,<sup>1</sup> Chitres Guria,<sup>1</sup> Ryan J.T. Nicholl,<sup>2</sup>

Sagar Chakraborty,<sup>1</sup> Kirill I. Bolotin,<sup>3</sup> and Saikat Ghosh<sup>1,\*</sup>

<sup>1</sup>*Department of Physics, Indian Institute of Technology - Kanpur, UP-208016, India*

<sup>2</sup>*Department of Physics and Astronomy, Vanderbilt University, Nashville, Tennessee 37235, USA*

<sup>3</sup>*Department of Physics, Freie Universität Berlin, Arnimallee 14, Berlin 14195, Germany*

(Dated: July 10, 2022)

**Can an atomically thin mechanical resonator render response of a resonator that is  $10^4$  times heavier than it, nonlinear? Here we find that strong back-action force of a freely suspended graphene drum resonator mode, with tunable coupling to a large area silicon nitride (SiNx) resonator results in nonlinear response of the significantly heavier and otherwise linear SiNx mode. Robust coupling of pristine graphene to SiNx substrate further amplifies the force. We develop a methodology based on observation of a novel frequency comb, to quantify nonlinear coefficients of these hybridized modes. We measure a giant induced nonlinear Duffing coefficient of  $\beta_{\text{hyb}}^s = 8.0(\pm 0.8) \times 10^{21}$  N/m<sup>3</sup>, on the SiNx resonator surface. Such ‘giant’, tunable nonlinearity induced in a high-Q SiNx resonator mode by graphene ‘cavity’ can find applications in precision measurements and in processing classical and quantum information with mechanical resonators.**

For more than a century, mechanical resonators [1] have played a central role in measuring new forces [2–4] and testing fundamental physical principles [5–8]. With the advent of microscale and nanoscale mechanical resonators, and in particular, after experimental observations of their quantum ground states [9–12], there has been a renewed interest in usage of such resonator modes as bits of information in classical [13] and quantum regimes [14, 15]. Accordingly, significant progress has been made in two broad directions over the last decade. On one hand, resonators with high quality factor ( $Q$ ) at high resonant frequency ( $f_0$ ) have been developed to get to a regime of  $Q \times f_0 \geq 10^{14}$  Hz where one expects to resolve their quantum states over classical fluctuations at room-temperature. Silicon Nitride (SiNx) has emerged as a dominant material of choice [16] for such resonators, demonstrating  $Q$ 's in excess  $10^7$  at MHz frequencies [17–19]. On the other hand, progress has been made in characterizing nonlinear response of mechanical modes, towards nonlinear phase shifting, controlled mixing, and processing bits of information [13]. Freely suspended graphene resonator—which has low mass and high Young's modulus [20–23] resulting in exceptionally nonlinear elastic properties—has been extremely efficient as a choice of material; mixing [24–30] and side-band cooling of its strongly coupled modes have been observed [31, 32]. Developing a platform that can integrate these two directions of progress, by combining high quality factors of SiNx resonators with strong nonlinear response of graphene resonators should therefore be the next logical step.

Here we explore a hybrid platform consisting of a large area SiNx resonator coupled to an atomically thin, freely suspended graphene that is deposited on holes etched on SiNx. We find that when a mechanical mode

of graphene is electrostatically tuned into resonance with a SiNx mode, the two resulting hybrid modes become nonlinear in their response to an external driving force (fig. 1a). To estimate the corresponding effective nonlinear coefficients of the hybrid modes, we drive the system parametrically and observe generation of a novel phase coherent frequency comb [24–30] in displacement power spectra. The comb carries unique signatures of nonlinear response of the hybrid modes. We develop a methodology to estimate Duffing constant and nonlinear damping of the hybrid modes from measured amplitudes of the frequency comb and our estimates match well with results of numerical modelling. The model suggests that giant induced nonlinearity [33] of the hybrid mode as measured on SiNx is due to a large back-action force from the low-mass and highly nonlinear graphene resonator that robustly couples to the SiNx resonator mode. Our results thereby combine two directions of development of electromechanical resonators in a single hybrid device, providing tunable nonlinear response of a relatively high-Q mechanical mode of a large area, heavy SiNx resonator (fig. 1a) [16].

## Nonlinear response of graphene-SiNx hybrid

The device consists of a 300 nm thick SiNx resonator of dimensions  $320 \times 320 \mu\text{m}^2$ , with through holes of diameters 10, 15, and 20  $\mu\text{m}$  etched on to it (fig. 1b) and monolayer (CVD) graphene is deposited on the holes [34]. Both graphene and SiNx resonators are actuated electrostatically with a highly doped silicon back gate, separated by 7  $\mu\text{m}$  insulator which results in net separation of 10  $\mu\text{m}$  between graphene and back gate. A fiber based confocal microscope, as part of a path stabilized Michelson interferometer, is used to detect optical signals reflected from the sample (3d cartoon of fig. 1a). Using thermal

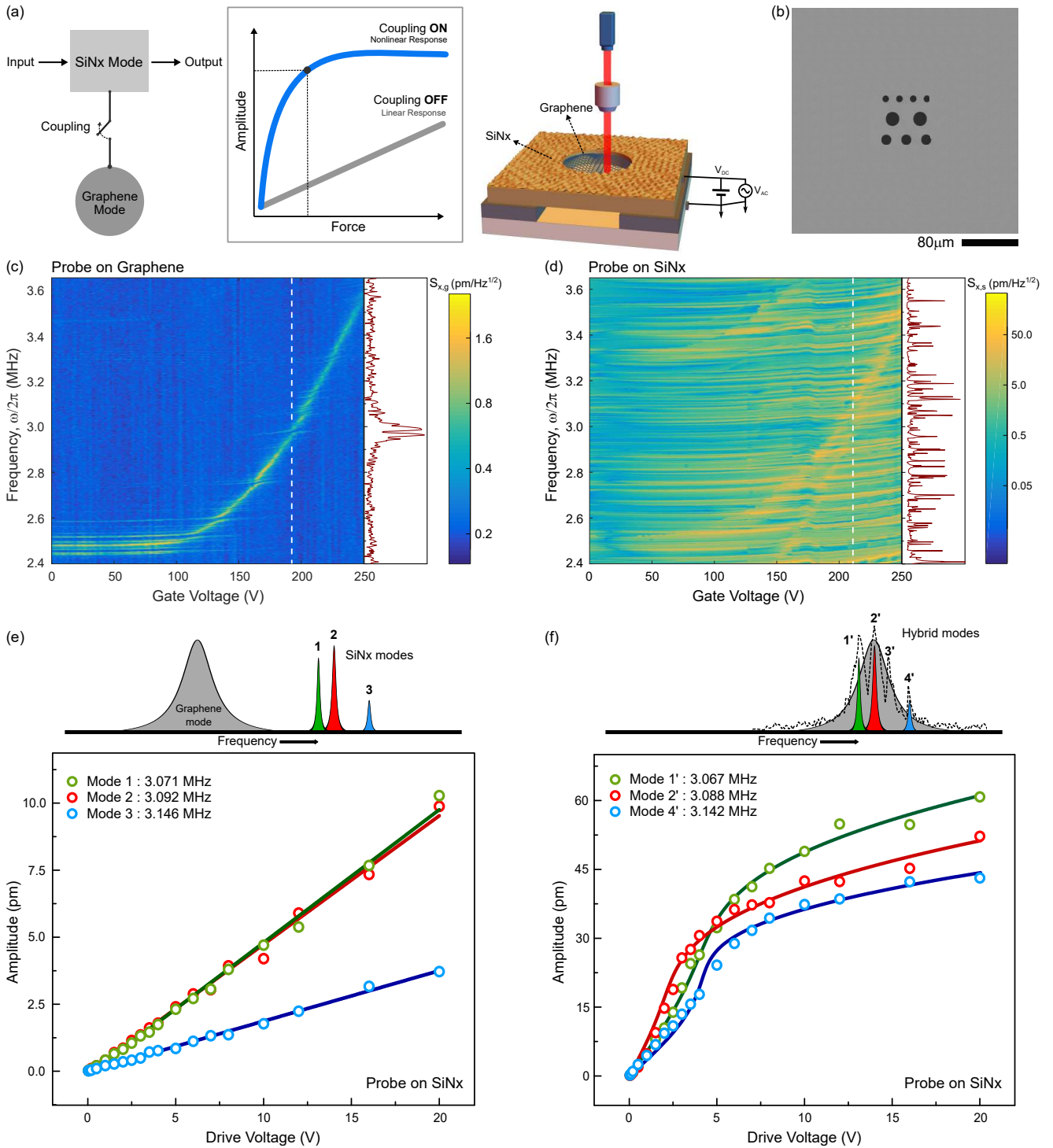


Figure 1: **Nonlinear response of graphene-SiNx modes:** (a) A cartoon depicting tunable, linear to nonlinear response of a SiNx resonator mode, due to its strong coupling to graphene. We observe oscillations of the hybrid mode with a confocal microscope, either focused on an atomically thin graphene or on the large area SiNx resonator surface (3d cartoon). (b) Scanning electron micrograph of the device with the large area SiNx resonator ( $320 \times 320 \times 0.3 \mu\text{m}^3$ , in grey) with graphene deposited onto 20, 15, and 10  $\mu\text{m}$  diameter holes etched on it. The 20  $\mu\text{m}$  diameter, intact graphene drum, coupling to SiNx is the focus of this study (see sec.III, S.I.). (c) Thermally driven 20  $\mu\text{m}$  graphene fundamental mode dispersion with the d.c. gate voltage interacting with array of SiNx modes. The right panel shows a cross-section at 194 V, where graphene hybridizes strongly with a single SiNx mode. (d) Corresponding dispersion of SiNx modes with dc gate voltage. The dispersion profile of fundamental modes of both the 20  $\mu\text{m}$  and the 15  $\mu\text{m}$  diameter graphene resonators can be observed, imprinted on SiNx dispersion, a signature of their backaction force. (e) Peak amplitude of three SiNx modes under direct a.c. drive shows linear response when not in resonance with the graphene mode. (f) When on resonance with low-Q graphene mode, response of the SiNx modes become nonlinear (dots). Solutions for steady-state amplitude of a Duffing oscillator fit well with the data points (solid line) (see sec. III-C, S.I.).

spectrum of graphene, we calibrate the power spectrum with a detection sensitivity of  $\sim 0.17 \text{ pm}/\sqrt{\text{Hz}}$ .

When the microscope is focused on a  $20 \text{ }\mu\text{m}$  freely standing graphene membrane, we observe thermally driven modes, corresponding to that of a circular resonator with anisotropic tension. The modes are tunable in excess of  $1 \text{ MHz}$  with a d.c. gate voltage (fig. 1c) and as we tune from  $0 \text{ V}$  to  $250 \text{ V}$ , we see distinct avoided level crossing that signals hybridization with modes of a SiNx resonator (fig. 1c and right panel). In a recent work we have found that a bilinear coupling model fits well with observed hybridized Brownian spectra and from that fitting, we extract the quality factors:  $Q_g \sim 254$  for graphene and  $Q_s \sim 3800$  for SiNx [35]. The effective mass of the graphene mode, estimated from dispersion of fig. 1c is estimated at  $m_g \sim 10m_0$ , where  $m_0$  is the mass of a single layer of graphene [35]. We estimate the effective mass,  $m_s$ , of SiNx from its dimensions and density, and find it to be  $\sim 10^4 m_g$  [35].

Comparatively heavier mass of SiNx results in smaller amplitude for the Brownian power spectrum, which is below our detection sensitivity (see sec. II, S.I.). However, when the device is actuated with a.c. gate voltage and the microscope is focused on SiNx away from graphene, we observe dense distribution of SiNx resonator modes (fig. 1d). The mode-densities and their dispersion (fig. 1d, right panel) match well with simulated modes of a square membrane of comparable dimensions with an in-built tension of  $80 \text{ MPa}$  (see sec.III-B, S.I.).

When SiNx modes are not hybridized with graphene, the peak amplitudes increase linearly with applied a.c. gate voltage, up to a maximum amplitude of  $20 \text{ V}$  that we can apply in our experiment. In particular, we measure three modes of SiNx at frequencies  $3.071 \text{ MHz}$  (mode 1),  $3.092 \text{ MHz}$  (mode 2), and  $3.146 \text{ MHz}$  (mode 3) as shown in fig. 1e. When the low-Q fundamental mode of graphene is tuned into resonance by applying a d.c. gate voltage  $V_g = 210 \text{ V}$ , we observe frequency shifts of the three modes ( $\sim 4 \text{ kHz}$ ) along with *nonlinear response* to the applied voltage (fig. 1f). The data fits well with the model of ref. [22], for the steady state amplitude ( $x_s$ ) of a forced oscillator with an additional nonlinear response that is cubic (Duffing) in  $x_s$ . From fitting, we extract the effective Duffing constant,  $\beta_{\text{hyb}}^s$ , for example, for the hybrid mode 2' to be  $\beta_{\text{hyb}2}^s = 8.0(\pm 0.8) \times 10^{21} \text{ N/m}^3$  (see sec.III-C, S.I. for the rest). From reported result for nonlinear threshold displacement of SiNx resonator ( $x_{\text{bare}}^{s,\text{cr}} = 1.2 \text{ }\mu\text{m}$  [4]), one can notice a giant five orders of magnitude reduction of threshold of the hybrid mode, at  $x_{\text{hyb}}^{s,\text{cr}} = 30.4 \text{ pm}$  (see sec. IV, S.I.).

### Towards understanding giant nonlinear coefficients

What leads to such giant Duffing constants for the hybridized SiNx modes? Aforementioned good fit to a

Duffing model of the SiNx hybrid mode implies that the third order response is due to its hybridization with graphene, a highly nonlinear Duffing oscillator. It is therefore critical to characterize the Duffing constant of our bare graphene resonator. We have indeed observed distinct signatures of Duffing-like hysteresis in response and asymmetric broadening due to nonlinear damping, when the graphene mode is driven hard at resonance with an a.c. gate voltage (see sec.III-A, S.I.). Recent studies have characterized Duffing coefficient and nonlinear damping of such driven graphene resonators by accurate fitting of data to theory [21, 22]. However, for our device, hybridization of a single graphene mode with multiple SiNx modes results in several free parameters, leading to large errors in the estimated Duffing constants from curve fitting. This calls for an alternative methodology to estimate nonlinear parameters.

### Parametric drive

The analysis of the system simplifies, when we drive the system parametrically at a frequency that is sum of two dominant hybrid modes (fig. 2a) [35]. The two-phonon resonant nature of the forcing specifically drives only two of the hybrid modes, leading to parametric gain having the other modes aside. Furthermore, novel spectroscopic signatures develop in the form of phononic comb. In rest of the letter, we develop a methodology based on observations and a model, to estimate Duffing constants of bare graphene as well as that of the hybrid modes as measured on graphene and on SiNx resonator surfaces. The parametric drive provides insights into the underlying nonlinear mechanism and the methodology based on the model provides a novel alternative technique, as opposed to curve fitting, to estimate  $\beta_{\text{hyb}}^s$  (fig. 1e).

To parametrically drive the system, we first tune the fundamental mode of graphene at a frequency,  $\omega_0 = 2.865 \text{ MHz}$ , at which it strongly hybridizes with a SiNx mode. With the microscope focused on the graphene, hybridization of modes is distinctly visible in the form of a splitting of the Brownian mode primarily into two modes, at frequencies, say,  $\omega_1$  and  $\omega_2$ . We simultaneously apply an a.c. gate voltage (parametric pump) at exactly twice the resonant frequency,  $\omega_0$  (fig. 2a). As the amplitude of the parametric pump voltage is increased, up to a threshold voltage  $V_c = 11.9 \text{ V}$  we observe gain in both the hybridized modes (see S.I. and [35]). Above this threshold, equispaced new frequency components on either side of the two hybridized modes emerge. The number of such modes increases with increasing pump voltage and eventually the modes span out into a ‘‘comb’’ like pattern with a triangular envelop (fig. 2b). The shape of the envelope is mildly asymmetric on either side of  $\omega_0$ . The separation between the modes decreases with the increasing pump voltage.

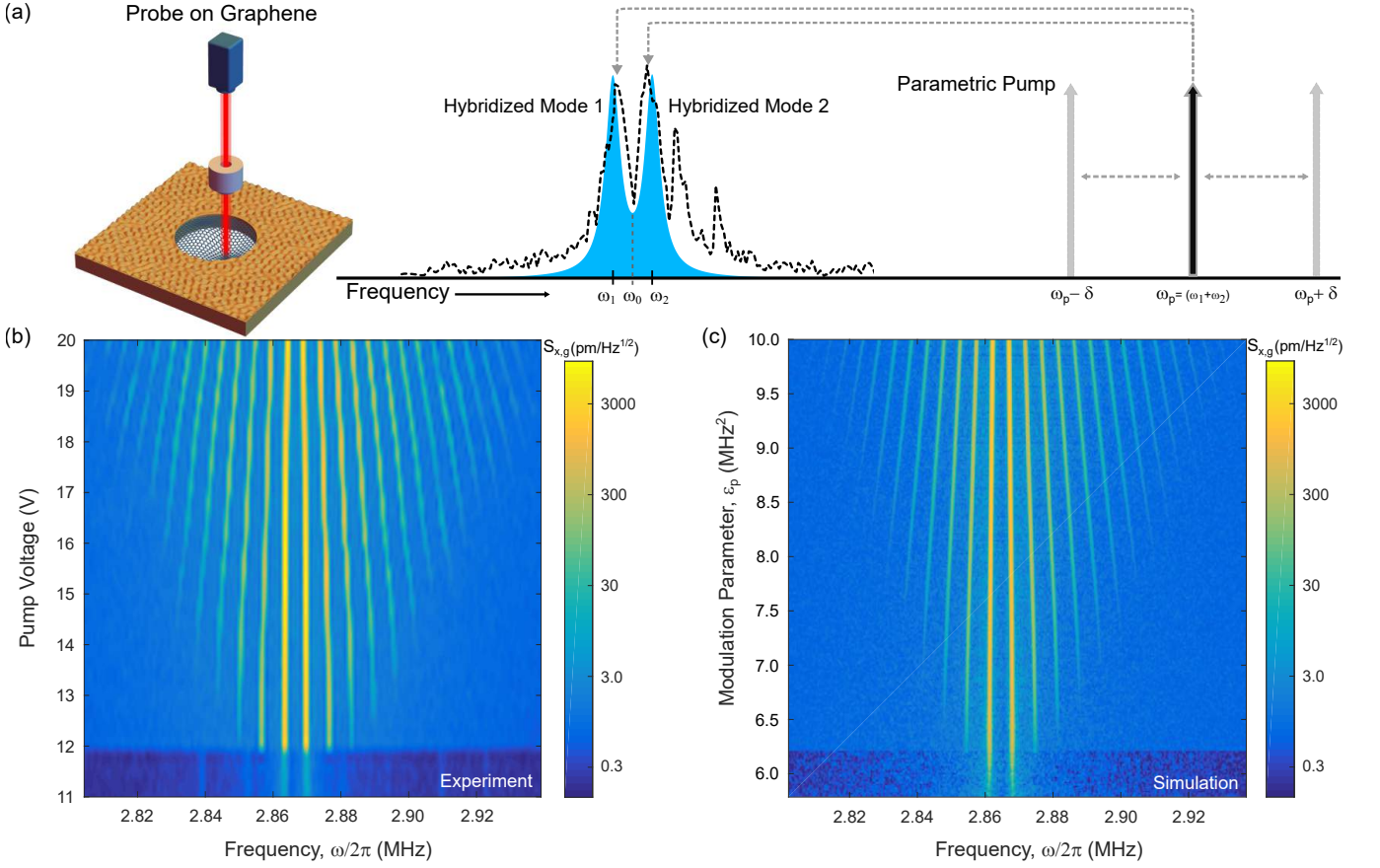


Figure 2: **Parametrically driven modes: on graphene.** (a) Cartoon depicting graphene-SiNx hybrid mode, probed on graphene, under parametric pumping at the sum of frequencies of the hybrid modes. Detuning of the pump from this resonance is defined as  $\delta$ . (b) Observation of phase coherent frequency comb in the parametrically instability regime, preceded by non-degenerate parametric amplification. The plot shows displacement power spectrum *measured on graphene*, with pump voltage scanned from 11 V to 20 V. (c) Corresponding numerical simulation of the coupled modes of linear SiNx and nonlinear graphene, driven with a parametric pump of strength  $\epsilon_p$  (see S.I.). Calibrating the amplitudes to fig. 2b gives an estimate of the Duffing constant and the nonlinear damping of the graphene.

### Theoretical model

Towards developing a functional understanding, we consider a model of graphene as a 1d oscillator with a quality factor  $Q_g$ , a third-order nonlinear response described by an effective Duffing constant ( $\beta_{\text{bare}}^g$ ) along with nonlinear damping ( $\eta_{\text{bare}}^g$ ) [21, 37, 38], coupled to a linear SiNx resonator mode. Specifically, we simulate the following set of equations:

$$\begin{aligned} \ddot{x}_g = & -\frac{\omega_g}{Q_g}\dot{x}_g - \frac{\eta_{\text{bare}}^g}{m_g}x_g^2\dot{x}_g - \frac{\beta_{\text{bare}}^g}{m_g}x_g^3 \\ & - [\omega_g^2 + \epsilon_p \cos(\omega_p t)]x_g - \frac{\alpha}{m_g}x_s, \end{aligned}$$

and

$$\ddot{x}_s = -\frac{\omega_s}{Q_s}\dot{x}_s - \omega_s^2 x_s - \frac{\alpha}{m_s}x_g.$$

Here  $\alpha$  is an effective coupling constant,  $x_{g,s}$  are the amplitudes of vertical displacements of graphene ( $g$ ) and

SiNx ( $s$ ) resonators modes respectively, and  $\epsilon_p$  denotes the magnitude of the parametric drive.  $\beta_{\text{bare}}^g$  is the Duffing constant of the bare graphene resonator mode while  $\eta_{\text{bare}}^g$  is the coefficient of nonlinear damping.

Features of numerically simulated spectra is in excellent agreement with the experimental observations (see sec. VI, S.I.). By fitting simulation to the calibrated spectra, we get an estimate for the Duffing constant of the bare (non-hybridized) graphene mode [23] to be  $\beta_{\text{bare}}^g = 5.8 \times 10^{13}$  N/m<sup>3</sup> with a nonlinear damping coefficient  $\eta_{\text{bare}}^g = 9.7 \times 10^6$  Ns/m<sup>3</sup>, in close agreement with recent measurements [22, 23].

Furthermore, experimentally measured comb spectra provides a direct means of quantifying nonlinear coefficients of the two hybrid modes (fig. 3). It is well understood that response of a parametrically driven oscillator mode becomes unstable above a threshold [39–42], above which, the instability regime extends to form a tongue

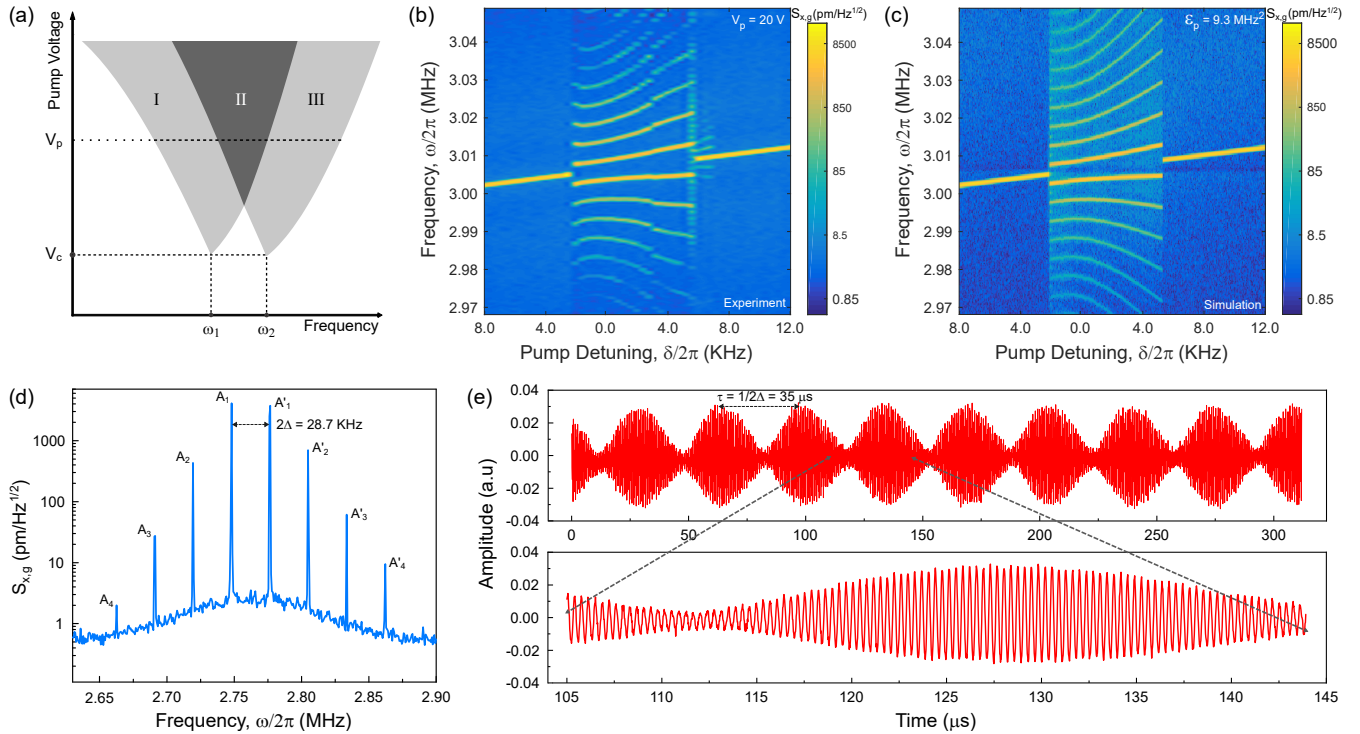


Figure 3: **Quantifying frequency comb:** (a) Cartoon of frequency response of a parametrically driven hybrid oscillator with two hybridized modes with frequencies  $\omega_1$  and  $\omega_2$ . Above a threshold, each mode develops a tongue shaped instability region. Accordingly one expects single frequency self-oscillation regimes (grey shades, I and III) while in the region of overlap, the system oscillates with two frequencies which mix to produce side bands (dark grey, region II). While the left edge of the envelope is due to the tongue of the hybridized mode  $\omega_1$ , the right edge is due to  $\omega_2$ . This insight leads to an estimation of the nonlinear coefficients of the hybrid modes. (b) To test the hypothesis of fig. 3a, we scan the pump frequency ( $\delta$ ) at a fixed a.c. pump voltage (black dashed line). We indeed observe a multi mode, comb spectra (region II) sandwiched between two single mode self-oscillation regimes (I and III). (c) Numerical simulation varying pump detuning matches well with the experimental observation. (d) Cross section of the multi-mode spectrum with mode separation of  $\sim 28.7$  KHz. From the ratios of amplitudes, we estimate nonlinear coefficients of the hybrid modes, *measured on graphene*. (e) Proof of phase coherence: measured time trace of the generated signal of fig. 3d shows a pulse sequence that is Fourier-transform limited, confirming that the pulse is phase coherent.

shaped region in the parameter space. The envelope of the tongue is set by pump amplitude, nonlinear frequency, and damping. Therefore, for the two hybridized modes—hybrid mode 1 and hybrid mode 2—respectively with frequencies,  $\omega_1$  and  $\omega_2$ , there should be two such independent instability tongues (fig. 3a). Consequently, there ought to be a region of overlap (dark region II, fig. 3a), [43]. While region I and region III correspond to self-oscillation of hybrid modes 1 and 2 respectively, in the overlap region II the system is multi-periodic with frequencies  $\omega_1$  and  $\omega_2$ . Moreover, in the instability region, large amplitude leads to strong nonlinear response. One therefore expects mixing of two accessible frequencies in the overlap region II.

The expected behaviour of the system in the aforementioned three regions is distinctly visible when we vary the pump frequency across  $\omega_p = 2\omega_0$  at a fixed drive amplitude,  $V_p$  (dotted line in fig. 3a) (fig. 2a). In particular, we scan the frequency over 20 kHz across  $2\omega_0$  keeping its amplitude fixed at  $V_p = 20$  V (fig. 3b). We indeed

observe single frequency self-oscillation regions I and III, on either side of region II that is characterised by the frequency comb (fig. 3b). As the final validation, we note that the experimental observations match well with numerical simulations (fig. 3c).

Diagram of fig. 3a therefore indicates that the right and the left boundaries of region II correspond to the instability tongues of the hybridized modes, viz., mode 1 and mode 2, respectively. One can then ascribe the observed asymmetry of the envelope of fig. 2b to that of different effective nonlinearities of the two hybrid modes. Furthermore, balancing the amplitudes of the new modes generated due to effective cubic nonlinearity ( $\beta_{\text{hyb1}}^g, \beta_{\text{hyb2}}^g$ ) and nonlinear damping ( $\eta_{\text{hyb1}}^g, \eta_{\text{hyb2}}^g$ ) with experimentally measured mode amplitudes  $a_i$  and  $a'_i$ , ( $i=1,2,\dots$ ), we estimate  $\beta_{\text{hyb1}}^g = 1.3(\pm 0.4) \times 10^{15}$  N/m<sup>3</sup>,  $\beta_{\text{hyb2}}^g = 8.6(\pm 4.6) \times 10^{14}$  N/m<sup>3</sup>,  $\eta_{\text{hyb1}}^g = 7.0(\pm 2.2) \times 10^7$  Ns/m<sup>3</sup>, and  $\eta_{\text{hyb2}}^g = 4.8(\pm 2.5) \times 10^7$  Ns/m<sup>3</sup> on average (see sec. IV, S.I.). We observe the estimated coefficients to de-

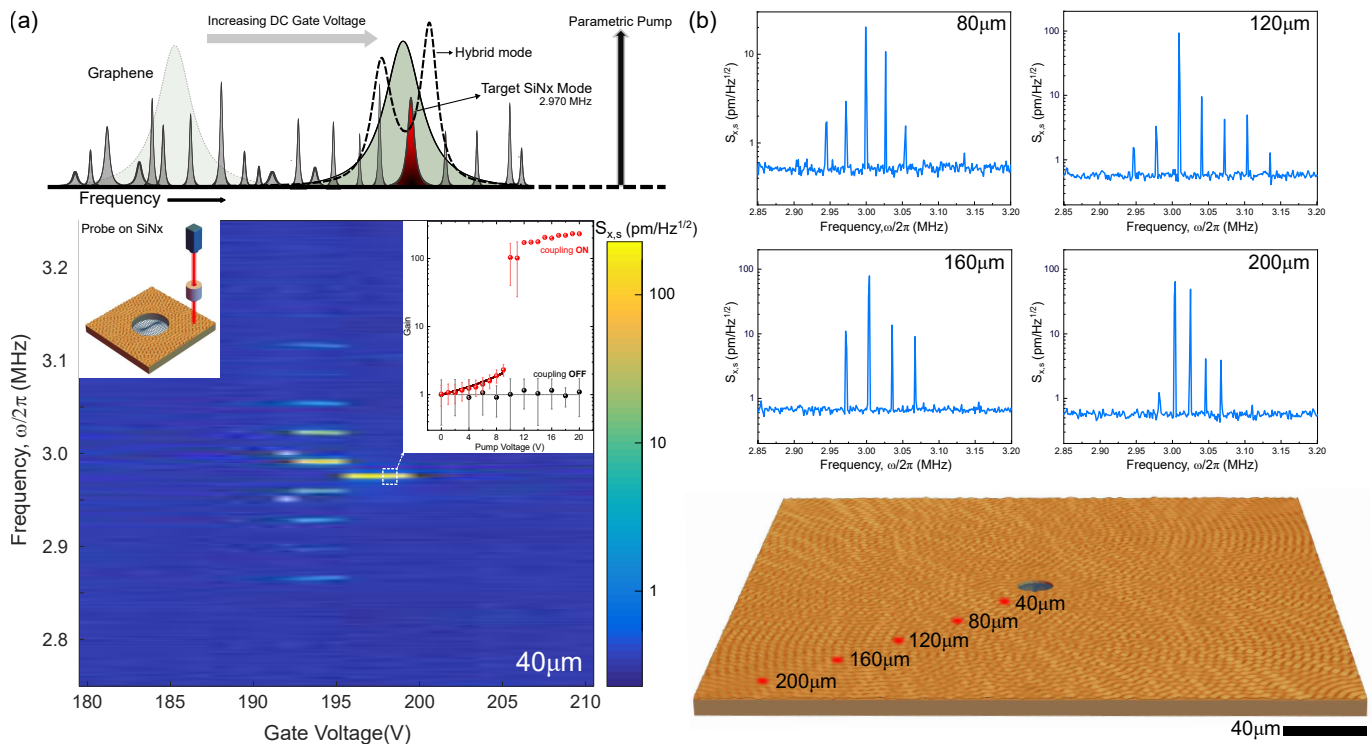


Figure 4: **Parametrically driven modes: on SiNx.** (a) When probed on SiNx, the measured displacement power spectra shows no response to our maximum parametric drive amplitude (inset). However, when a graphene mode is tuned into resonance, we observe parametric gain below a threshold (inset), along with generation of the frequency comb. We again use the comb lines to estimate nonlinear coefficients of the hybrid, as measured on SiNx resonator. (b) As we move the microscope away from graphene remaining focused on SiNx, we observe nonlinear response the hybrid modes leading to multimode spectrum at far distances (4 measurements shown as red spots on a device cartoon along with one at  $40\mu\text{m}$  on left, fig. 4a). Nonlinear response of the hybrid modes, for such small displacements of the SiNx surface, results in a giant Duffing constant  $\beta_{\text{hyb}}^s$  for SiNx.

pend on the pump voltage and this dependence, along with the estimations from data, are in good agreement with numerical simulations (see S.I.). This substantiates our methodology for estimating and quantifying the effective nonlinear coefficients of the two hybrid modes.

There is a definite nonlinear phase relationship of the generated modes with respect to the fundamental modes, at frequencies  $\omega_{1,2}$ , and in principle, the nonlinear coefficients can also be estimated by carefully measuring relative phases of the generated modes. For the spectrum of fig. 3d, we observe pulses in time domain (fig. 3e). Repetition rate of the pulses correspond to inverse of  $2\Delta = \omega_1 - \omega_2$ , pulse width to inverse of the envelope of the generated comb while the carrier frequency to inverse of the carrier frequency  $\omega_0 = 2.760\text{ MHz}$  (fig. 3d). The frequency comb of the hybrid mode is therefore phase coherent and Fourier transform limited.

It can be noted that due to widely varying masses and quality factors of the two physical resonators, values of Duffing coefficients of a hybrid mode would differ when measured on graphene or on SiNx resonator surface (see sec. V, S.I.). Interestingly, signature of the comb spectrum is also observable, when the microscope

is focused on the surface of the SiNx resonator (fig. 4). However, the amplitude of oscillations is orders of magnitude smaller than that on graphene, due to significantly heavier mass of SiNx. Accordingly, signatures of measured spectrum are less pronounced. Nevertheless, we use the developed methodology to estimate Duffing coefficients of the hybrid modes on SiNx. In fig. 4, we focus on a SiNx mode at  $2.970\text{ MHz}$ , while applying a parametric drive at twice its resonant frequency. When the fundamental graphene mode is off-resonant, we do not observe any parametric gain (blue region on the left of fig. 4a and black dots in the right inset). However, when the graphene mode is tuned across resonance with a gate voltage between  $193\text{ V}$  (approx.) to  $200\text{ V}$ , we observe generation of frequency comb as well as single frequency self-oscillation regime. Furthermore, the induced nonlinearity of the hybrid mode extends over the entire SiNx surface and we observe generation of combs at distances in excess of  $200\mu\text{m}$  from the edge of the graphene drum that is only  $20\mu\text{m}$  in diameter (fig. 4b, bottom panel). Essentially, the localized mode of the graphene acts as a defect center, on the large area oscillating mode of SiNx.

From amplitudes of the generated modes, we estimate the effective Duffing constant and nonlinear damping of the hybrid modes to be  $\beta_{\text{hyb1}}^s = 3.4(\pm 0.1) \times 10^{23}$  N/m<sup>3</sup>,  $\beta_{\text{hyb2}}^s = 6.3(\pm 5.3) \times 10^{22}$  N/m<sup>3</sup> and  $\eta_{\text{hyb1}}^s = 1.8(\pm 0.1) \times 10^{16}$  Ns/m<sup>3</sup>,  $\eta_{\text{hyb2}}^s = 3.3(\pm 2.8) \times 10^{15}$  Ns/m<sup>3</sup> respectively, as measured on SiNx surface (see sec. VI, S.I.). The estimates are in close agreement with effective Duffing constant  $\beta_{\text{hyb}}^s$  measured on SiNx in fig. 1f.

## Conclusion

To conclude, here we have explored nonlinear response of graphene-SiNx hybrid modes and developed a methodology to quantify corresponding nonlinear coefficients, as measured on graphene and SiNx resonator surfaces. The measured Duffing constant of the hybrid mode on SiNx surface is found to be nine orders of magnitude larger than that on graphene. This indicates that nonlinear response is highly efficient on SiNx surface, setting in at displacement scale that is two orders of magnitude smaller, at 40 pm, compared to measurement on graphene.

It is remarkable that an atomically thin resonator generates a significant backaction force ( $F^{\text{ba}} = \alpha x_g$ ) on SiNx. Based on the  $F^{\text{ba}}$ , a perturbative estimate yields  $\beta_{\text{hyb}}^s \propto \alpha \beta_{\text{bare}}^g / m_g^2$  (see sec. V, S.I.) and indicates graphene to be a powerful candidate to induce such giant nonlinearity due to three primary factors: firstly, pristine graphene robustly couples to SiNx substrate via stable electrostatic forces resulting in a large coupling strength ( $\alpha$ ). This also leads to better device yield. Secondly, low mass of graphene ( $m_g$ ) results in a large amplitude ( $x_g$ ) of oscillation, boosting the force further. Finally, exceptionally large Young's modulus results in large nonlinear response ( $\beta_{\text{bare}}^g$ ) [22] to an applied force. Large tunable backaction force of graphene thereby emerges as the dominant mechanism behind observations in this work.

For our device, the tension of SiNx resonator is merely 80 MPa [16], leading to comparatively lower quality factors ( $\sim 3000$  on average), along with a dense distribution of SiNx modes (fig. 1d). An immediate improvement can therefore be towards increasing inbuilt tension of the SiNx resonator, so that one can resolve mode shapes distinctly and observe graphene induced interaction between SiNx modes of quality factors in excess of  $10^6$ , possibly in a quantum regime. With this improvement, the hybrid device proposed here can provide a new platform for generating nonlinearity induced mechanical squeezed states in precision measurements and for controlled nonlinear phase shifts in long lived mechanical bits of information, both in classical and quantum domains at room temperature.

surement, Cambridge University Press, Cambridge.

- [2] Weber, P. *et. al.* Force sensitivity of multilayer graphene optomechanical devices. *Nature communications* **7**, 12496 (2016).
- [3] Cavendish, H. Experiments to Determine the Density of the Earth. *Philosophical Transactions of the Royal Society of London* **88**, 469-526 (1798).
- [4] Abbott, B. P. *et. al.* Observation of Gravitational Waves from a Binary Black Hole Merger. *Phys. Rev. Lett.* **116**, 061102 (2016).
- [5] Clerk, A. A., Devoret, M. H., Girvin, S. M., Marquardt, F. & Schoelkopf, R. J. Introduction to quantum noise, measurement, and amplification. *Rev. Mod. Phys.* **82**, 1155 (2010).
- [6] Wollman, E. E. *et. al.* Quantum squeezing of motion in a mechanical resonator. *Science* **349**, 952-955 (2015).
- [7] Ockeloen-Korppi, C. F. *et. al.* Stabilized entanglement of massive mechanical oscillators. *Nature* **556**, 478482 (2018).
- [8] Marinkovi, I. *et. al.* Optomechanical Bell Test. *Phys. Rev. Lett.* **121**, 220404 (2018).
- [9] Teufel, J. D. *et. al.* Sideband cooling of micromechanical motion to the quantum ground state. *Nature* **475**, 359363 (2011).
- [10] Schliesser, A. *et. al.* Resolved-sideband cooling of a micromechanical oscillator. *Nature* **4**, 415419 (2011).
- [11] Aspelmeyer, M., Kippenberg, T. J. & Marquardt, F., Cavity optomechanics. *Rev. Mod. Phys.* **86**, 1391 (2014).
- [12] OConnell, A. D. *et. al.* Quantum ground state and single-phonon control of a mechanical resonator. *Nature* **464**, 697703 (2010).
- [13] Mahboob, I. *et. al.* Interconnect-free parallel logic circuits in a single mechanical resonator. *Nature Comm.* **2**, 198 (2011).
- [14] Rips, S. & Hartmann, M. J. Quantum Information Processing with Nanomechanical Qubits. *Phys. Rev. Lett.* **110**, 120503 (2013).
- [15] Mika A. Sillanpää *et. al.* Coherent quantum state storage and transfer between two phase qubits via a resonant cavity *Nature* **449**, 438442 (2007).
- [16] Fink J.M. *et. al.* Quantum electromechanics on silicon nitride nanomembranes. *Nature Communications* **7**, 12396 (2016).
- [17] Reinhardt, C., Müller, T., Bourassa, A. & Sankey, J. C. Ultralow-Noise SiN Trampoline Resonators for Sensing and Optomechanics. *Phys. Rev. X* **6**, 021001 (2016).
- [18] Norte, R. A., Moura, J. P. & Gröblacher, S. Mechanical Resonators for Quantum Optomechanics Experiments at Room Temperature. *Phys. Rev. Lett.* **116**, 147202 (2016).
- [19] Patil, Y. S. *et. al.* Thermomechanical Two-Mode Squeezing in an Ultrahigh-Q Membrane Resonator. *Phys. Rev. Lett.* **115**, 017202 (2015).
- [20] Lee, C., Wei, X., Kysar, J. W & Hone, J. Measurement of the Elastic Properties and Intrinsic Strength of Monolayer Graphene. *Science* **321**, 385-388 (2008).
- [21] Eichler, A. *et. al.* Nonlinear damping in mechanical resonators made from carbon nanotubes and graphene. *Nature Nanotechnology* **6**, 339342 (2011).
- [22] Davidovikj, D. *et. al.* Nonlinear dynamic characterization of two-dimensional materials *Nature Comm.* **8**, 1253 (2017).
- [23] Storch, I. R. *et. al.* Young's modulus and thermal expansion of tensioned graphene membranes *Physical Review B* **98** (8), 085408 (2018).

\* Electronic address: gsaiikat@iitk.ac.in

[1] Braginsky, V. B. & Khalili, F. Y., 1992, Quantum Mea-

- [24] Karabalin, R. B., Cross, M. C., Roukes, M. L. Nonlinear dynamics and chaos in two coupled nanomechanical resonators. *Phys. Rev. B* **79**, 165309 (2009).
- [25] Mahboob, I. *et. al.* Tunable electromechanical comb generation *Appl. Phys. Lett.* **100**, 113109 (2012).
- [26] Cao, L. S. *et. al.* Phononic Frequency Combs through Nonlinear Resonances. *Phys. Rev. Lett.* **112**, 075505 (2014).
- [27] Mahboob, I. *et. al.* Hopf and period-doubling bifurcations in an electromechanical resonator. *Appl. Phys. Lett.* **109**, 073101 (2016).
- [28] Ganesan, A., Do, C., & Seshia, A. Phononic Frequency Comb via Intrinsic Three-Wave Mixing. *Appl. Phys. Lett.* **118**, 033903 (2017).
- [29] Ganesan, A., Do, C., & Seshia, A. Phononic frequency comb via three-mode parametric resonance. *Phys. Rev. Lett.* **112**, 021906 (2018).
- [30] Czaplewski, D. A. *et. al.* Bifurcation Generated Mechanical Frequency Comb. *Phys. Rev. Lett.* **121**, 244302 (2018).
- [31] Alba, R. D. *et. al.* Tunable phonon-cavity coupling in graphene membranes. *Nat. Nano.* **11**, 741 (2016).
- [32] Mathew, J. P. *et. al.* Dynamical strong coupling and parametric amplification of mechanical modes of graphene drums. *Nat. Nano.* **11**, 747 (2016).
- [33] Huang, P. *et. al.* Generating giant and tunable nonlinearity in a macroscopic mechanical resonator from a single chemical bond *Nature Comm.* **7**, 11517 (2016).
- [34] Nicholl, R. J. T. *et. al.* The effect of intrinsic crumpling on the mechanics of free-standing graphene. *Nat. Commun.* **6**, 8789 (2015).
- [35] Singh, R., Nicholl, R. J. T., Bolotin, K. I. & Ghosh, S. *et. al.* Motion Transduction with Thermo-mechanically Squeezed Graphene Resonator Modes. *Nano Lett.* **18** (11), 6719-6724 (2018).
- [36] Zwickl, B. M. *et.al* High quality mechanical and optical properties of commercial silicon nitride membranes *Applied Physics Letters* **92**, 103125 (2008).
- [37] Lifshitz, R. & Cross, M. C. Review of Nonlinear Dynamics and Complexity. Wiley-VCH (2009).
- [38] Nayfeh, A. H., Mook, D. T. 2007, Nonlinear Oscillations, WILEYVCH Verlag GmbH & Co. KGaA.
- [39] Rand, R. H. Lecture Notes on Nonlinear Vibrations (2012).
- [40] Landau, L. D. & Lifshitz, E. M. 1982, Mechanics: Volume 1 (Course of Theoretical Physics ), Butterworth-Heinemann; 3 edition.
- [41] Hsu, C. S. On the parametric excitation of a dynamic system having multiple degrees of freedom. *J. Appl. Mech.* **30**, 367-374 (1963).
- [42] Kovacic, I., Rand, R. & Sah, S.M. Mathieu's Equation and Its Generalizations: Overview of Stability Charts and Their Features. *Appl. Mech. Rev* **70**(2), 020802 (2018).
- [43] Hansen, J. Stability diagrams for coupled Mathieu equations. *Ing. arch* **55**, 463-473 (1985).

### Acknowledgment:

We thank Srivatsan Chakram, Deb Shankar Ray, Edgar Knobloch, Siddharth Tallur, Mandar Deshmukh and Amit Agarwal for insightful discussions and comments. We also thank Om Prakash for his numerous help in construction of the experimental setup. This work was supported under DST grant no: SERB/PHY/2015404 and ERC Grant No. 639739.

### Method:

#### *Experimental setup:*

Motion of graphene and SiNx mechanical resonators are detected with a confocal microscope (spot-size of 4  $\mu\text{m}$ ), using a probe laser (ECDL, Toptica) at a wavelength of 780 nm. The microscope forms one arm of a Michelson interferometer while a second (reference) arm is actively stabilized using PI lock box to counter ambient vibrations. The probe, derived from a frequency and power stabilized external cavity diode laser, is detected with a balanced photo-detector of bandwidth of 45 MHz. Subsequently, a spectrum analyser (Lock in) is used to detect (drive) displacement power spectrum of the graphene or SiNx target resonator. The sample is placed in a rough vacuum chamber (at a pressure of  $\sim 10$  mTorr), along with high voltage gate contacts at room temperature. The chamber in turn is placed on a 3D scanning stage (Thorlabs) having active position locking, with a closed-loop position stability of 5 nm.

#### *Sample Preparation:*

SiNx membranes (thickness 300 nm) are fabricated by depositing low-stress silicon-rich silicon nitride on both sides of a silicon chip. An array of holes of 15 and 20  $\mu\text{m}$  diameter is then patterned in the nitride using standard fabrication procedures. A metallic contact (20 nm Au) is deposited onto the top surface of the SiN to facilitate electrical gating. Monolayer chemical vapor deposition (CVD) graphene is then transferred onto holes in the nitride membranes. We use a high-quality atmospheric CVD growth and wet transfer. The samples are subsequently annealed in an  $Ar - H_2$  environment at  $350^\circ\text{C}$ . The graphene membranes remained clamped to the sample chip via van der Waals interactions forming suspended circular graphene membranes.

# Supplementary Information: Giant Tunable Mechanical Nonlinearity in Graphene-Silicon Nitride Hybrid Resonator

## I. Experimental method

**Experimental Setup:** We use a fiber based confocal microscope with a spot size of  $4\ \mu\text{m}$  to optically probe the graphene-SiN<sub>x</sub> hybrid device. The microscope forms one arm of a Michelson interferometer while the reference arm is actively stabilized against drifts or fluctuations through a feedback loop and PI lock. A frequency and amplitude stabilized external cavity diode laser (ECDL) ( $\lambda = 780\ \text{nm}$ ) is used as an optical probe. The sample is placed inside a vacuum chamber ( $10^{-2}\ \text{mbar}$ ) with high voltage electrical leads for gate control. The entire chamber assembly is mounted on a 3D scanning stage with active position locking. Fig. S.1 below illustrates the experimental setup.

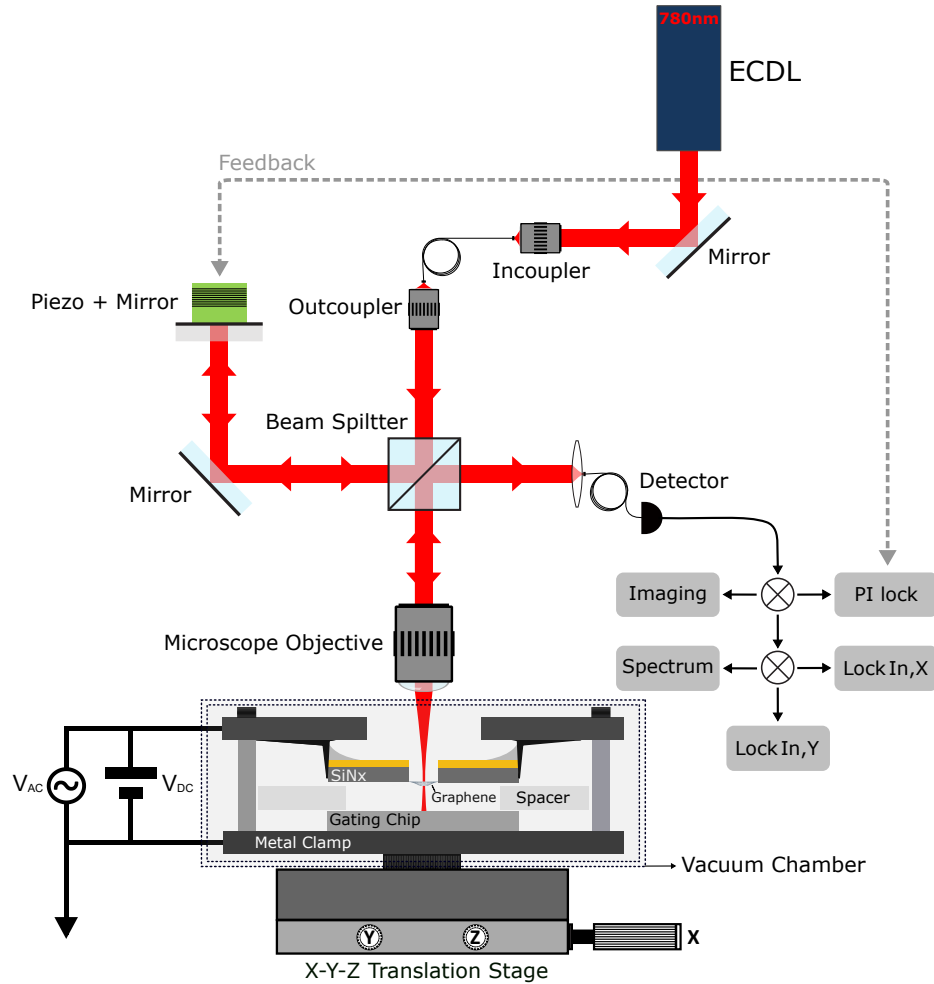


Figure S.1: **Experimental Setup.**

For detection, we use a balanced photo-detector with a detection bandwidth of 45 MHz. We position the sample by actively monitoring the generated 2-d confocal image, which helps in selecting the relative probe position and to lock the microscope there. The photo-current signal is analysed with spectrum analyzer and dual-lock-in-amplifier. Fig. 1c, 2b, 3b, 3d, 4a and 4b in the main text and S. 2, S. 11 and S. 14 in the supplement are taken with spectrum analyzer while fig. 1d-f in the main text and S. 3-6 and S. 16 in the supplement are acquired by scanning the drive frequency from a lock-in-amplifier.

## II. Displacement calibration from hybrid Brownian spectrum

Our model is based on coupled modes of graphene and SiNx resonators, denoted by 1-dimensional displacement  $x_g$  and  $x_s$ , respectively. For thermally driven graphene and SiNx modes we can ignore the nonlinear terms. The equations of motion are given by:

$$\ddot{x}_g + \gamma_{bare}^g \dot{x}_g + \omega_g^2 x_g - \frac{\alpha}{m_g} x_s = \frac{F_g^{th}}{m_g} \quad (\text{S.1a})$$

and

$$\ddot{x}_s + \gamma_{bare}^s \dot{x}_s + \omega_s^2 x_s - \frac{\alpha}{m_s} x_g = \frac{F_s^{th}}{m_s}, \quad (\text{S.1b})$$

where  $\gamma_{bare}^k$ ,  $\omega_k$  and  $F_k^{th}$  ( $k = g, s$ ) represent linear damping, normal mode frequency and thermal forces acting on graphene and SiNx modes respectively. The graphene mode is bilinearly coupled to a SiNx mode which is modeled by an effective interaction Hamiltonian,  $H_{int} = \alpha x_g x_s$ , where  $\alpha$  is a coupling constant. Solving the above coupled equations in the fourier space, displacement power spectrum for the graphene resonator takes the following form:

$$S_{x,g}^{1/2} = \left[ \kappa \left( \frac{\frac{S_{F,g}^{th}}{m_g^2} \{(\omega_g^2 - \omega^2)^2 + (\gamma_{bare}^g)^2 \omega^2\} + \{ \frac{S_{F,s}^{th} \alpha^2}{m_s^2 m_g^2} \}}{[(\omega_g^2 - \omega^2)(\omega_s^2 - \omega^2) - \gamma_{bare}^g \gamma_{bare}^s \omega^2 - \frac{\alpha^2}{m_g m_s}]^2 + [(\omega_g^2 - \omega^2) \gamma_s \omega + (\omega_s^2 - \omega^2) \gamma_{bare}^g \omega]^2} \right) + S_{noise} \right]^{1/2}, \quad (\text{S.2})$$

where  $S_{F,k} = 4k_B T \gamma_{bare}^k$ , ( $k = g, s$ ) is the thermal force acting on graphene ( $g$ ) and SiNx ( $s$ ). The calibration factor,  $\kappa$  along with several parameters are extracted by fitting experimental data,  $S_{v,g}^{1/2} (\text{V}/\sqrt{\text{Hz}})$  to the above equation. The recorded spectrum is converted into displacement spectrum,  $S_{x,g}^{1/2} (\text{m}/\sqrt{\text{Hz}})$  by dividing with  $\sqrt{\kappa}$ .

The extracted values of the fitting parameters for the brownian mode corresponding to fig. S.2 are listed below.

$\kappa = 1.921(\pm 0.074) \times 10^{10} \text{ V}^2/\text{m}^2$ ,  $\omega_g/2\pi = 2.8646(\pm 0.0002) \times 10^6 \text{ Hz}$ ,  $\omega_s/2\pi = 2.8656(\pm 0.0001) \times 10^6 \text{ Hz}$ ,  $\gamma_{bare}^g/2\pi = 11.237(\pm 0.690) \times 10^3 \text{ Hz}$ ,  $\gamma_{bare}^s/2\pi = 0.744(\pm 0.234) \times 10^3 \text{ Hz}$ ,  $\alpha/4\pi^2 = 1.978(\pm 0.095) \times 10^{-3} \text{ kgHz}^2$ .

This model can be extended for graphene interaction with multiple SiNx modes. The supplemental information of Singh, R. et.al. [1] can be referred for more information.

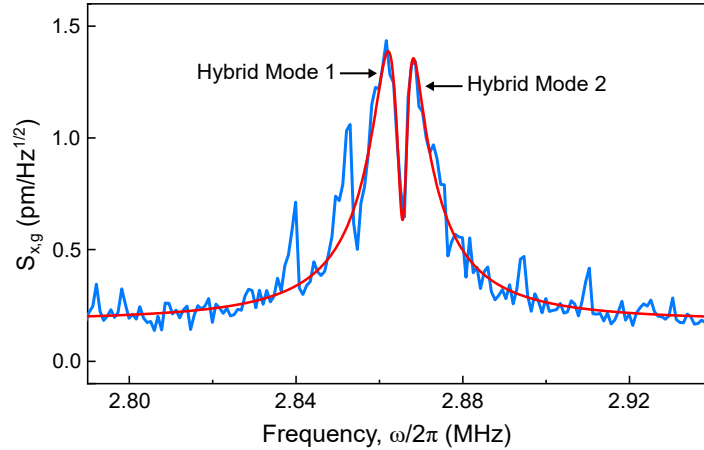


Figure S.2: Brownian spectrum of coupled mode of graphene-SiNx hybrid fitted with equation S.2.

### III. Graphene and Silicon Nitride resonator modes

#### A. Nonlinear modes of Graphene resonator

The sample consists of a large area SiNx resonator ( $320 \times 320 \times 0.3 \mu\text{m}^3$ ), with  $20 \mu\text{m}$ ,  $15 \mu\text{m}$  and  $10 \mu\text{m}$  diameter circular holes etched on to it over which monolayer graphene has been deposited, thereby forming drums that are clamped to SiNx at the edges via Van der Waals forces while its rest of the part is freely hanging. When the microscope is focused on graphene, we observe its thermal spectrum in the electronic spectrum analyser.

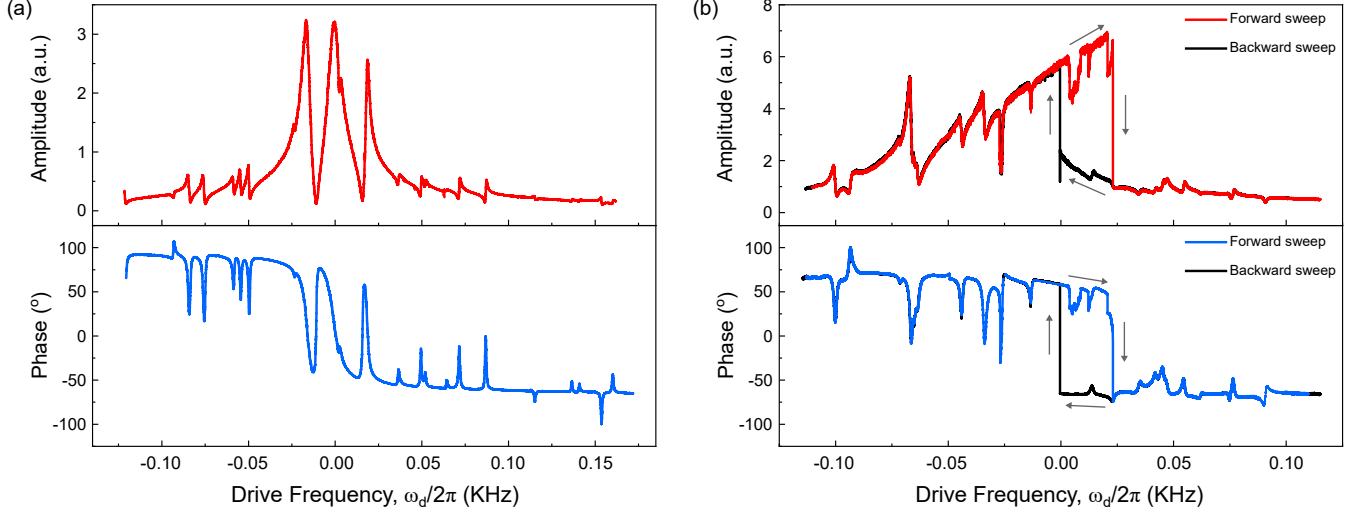


Figure S.3: **Nonlinearity of hybridized graphene modes:** (a) Amplitude plot of weakly driven (linear regime) graphene fundamental mode that is interacting with multiple SiNx modes and its corresponding phase profile. (b) At larger drive, spectrum shows asymmetric profile with hysteresis, a quintessential signature of cubic nonlinearity.

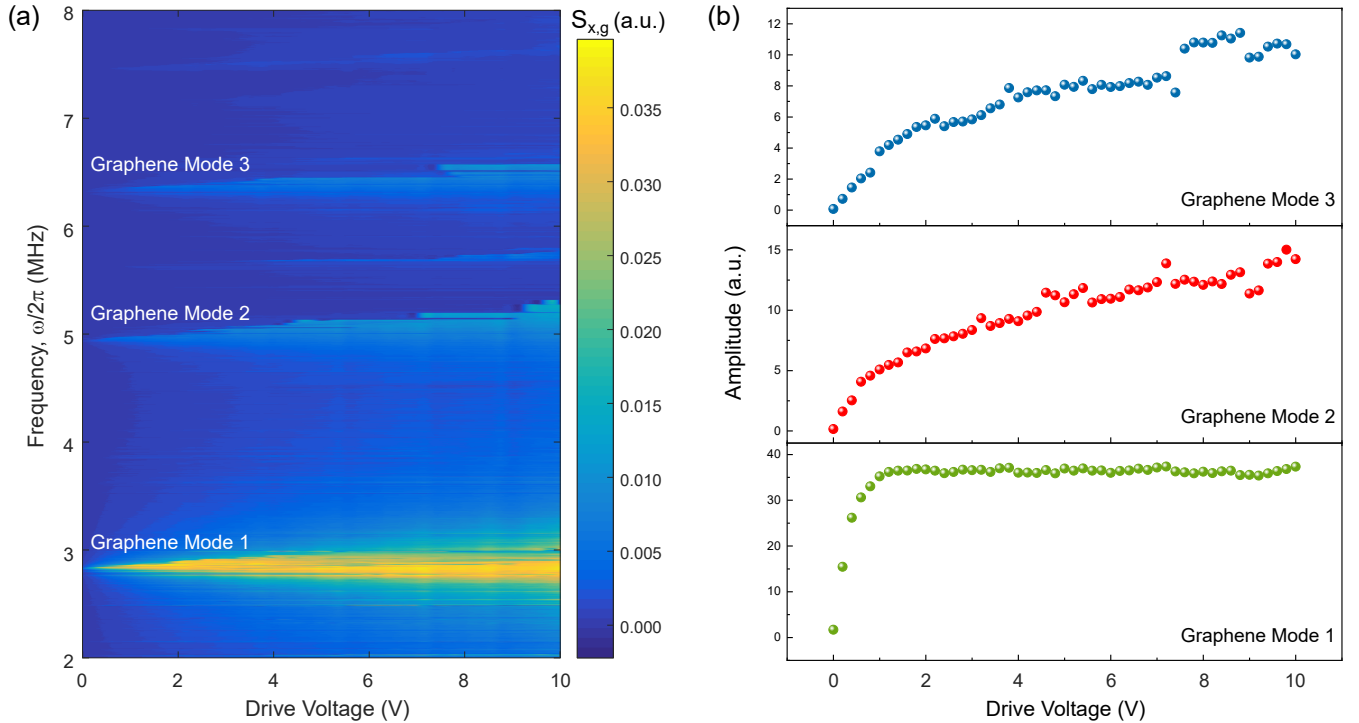


Figure S.4: **Nonlinear damping and saturation of amplitude of graphene modes:** (a) Spectrum of graphene modes as a function drive voltage. (b) The amplitude of graphene modes as a function of drive voltage.

Fig. 1c (main text) shows the dispersion of fundamental mode of graphene as a function of changing tension of the graphene membrane via dc gate voltage. Mode profiles deviate from an expected Lorentzian shape, due to its interaction with densely packed, multiple SiNx modes. Such interactions lead to sharp dips and Fano-like asymmetry in graphene spectrum (fig. S.3a). The asymmetry gets more pronounced in when the graphene mode is driven on resonance. The corresponding phase profile shows an overall envelop of  $\pi$ -phase flip when we go through the broad graphene resonance. However, the finer features in the phase profile with sharp  $\pi$  phase flips, correspond to individual SiNx modes which are coupled to the graphene mode with varying coupling strengths.

When driven harder, graphene shows a typical asymmetric signature that is typical of a Duffing oscillator with cubic nonlinear response in displacement (fig. S.3b). Forward and backward sweeps of drive frequency shows hysteresis in both the amplitude and phase.

Fig. S.4a shows transition from a linear response to a Duffing-like nonlinear response for the graphene mode, coupled to multiple SiNx modes. The spectrum shows an increase in the (full width at half maximum) FWHM with increasing drive voltage, pointing towards the existence of nonlinear damping. The amplitude of the graphene modes with drive voltage show saturation after a certain drive voltage and the critical voltage for saturation is specific to a given mode (fig. S.4b).

### B. Modes of large area Silicon Nitride resonator

Silicon Nitride is a large area ( $320 \times 320 \times 0.3 \mu\text{m}^3$ ) resonator with through holes. Fig. S.5 shows the amplitude and phase of weakly driven SiNx modes. The modes are densely packed with quality factor in the range of 1000-4000. From COMSOL simulation, we estimate the inbuilt tension,  $T_s \sim 80$  MPa.

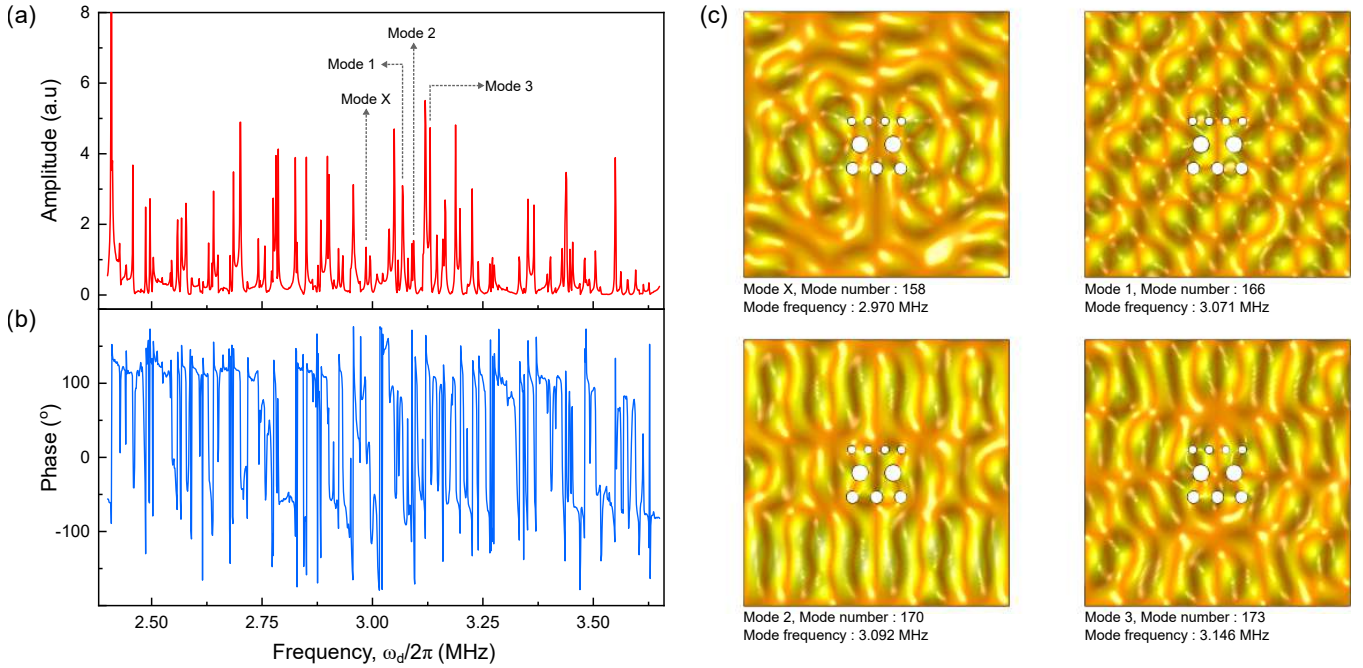


Figure S.5: **Silicon Nitride Modes:** (a) Amplitude of driven SiNx modes. In particular the modes X, 1, 2 and 3 and their interaction with the fundamental graphene mode were studied in detail. (b) Corresponding phase profile of the SiNx modes. The small mode spacing between the adjacent modes is due to the low inbuilt tension in SiNx resonator. (c) Spatial profiles of modes X, 1, 2 and 3 indicated with their mode number and frequency respectively. Simulation of the spatial profiles were done in COMSOL Multiphysics 5.2.

### C. Nonlinear response of hybrid Silicon Nitride modes under direct driving

We observe a driven SiNx mode, when far detuned from graphene mode, respond linearly to an applied forcing (via ac gate voltage). However, for a SiNx mode coupled to a graphene mode, its response is nonlinear and shows saturation

in amplitude above a critical displacement. We first calibrate the SiNx amplitude (23.7 fm) at 20 mV drive voltage, by carefully comparing it with the calibration value of graphene's Brownian spectrum, keeping all other detection parameters constant.

To quantify nonlinear response of the SiNx modes, we follow the procedure described in D. Davidovikj et.al. [2]. We first extract the *slope* from the linear region of  $x_s$  vs  $V_{ac}$  plot (fig. 1e, main text). The rescaled force  $F$  corresponding to the  $V_{ac}$  is given by,

$$F = slope \frac{\omega_s^2 m_s}{Q_s} V_{ac}. \quad (\text{S.3})$$

This rescaled force is plotted with  $x_s$ , the steady-state response of a Duffing oscillator, such that [2]:

$$\zeta F = (Ax^2 + Bx^4 + Cx^6)^{1/2} \quad (\text{S.4})$$

where  $C = \frac{9}{16}(\beta_{hyb}^s)^2$ . Here  $\zeta$  depends on the geometry of the mode and is of the order of 1. We fit this equation to Fig. S6 and extract  $C$ .

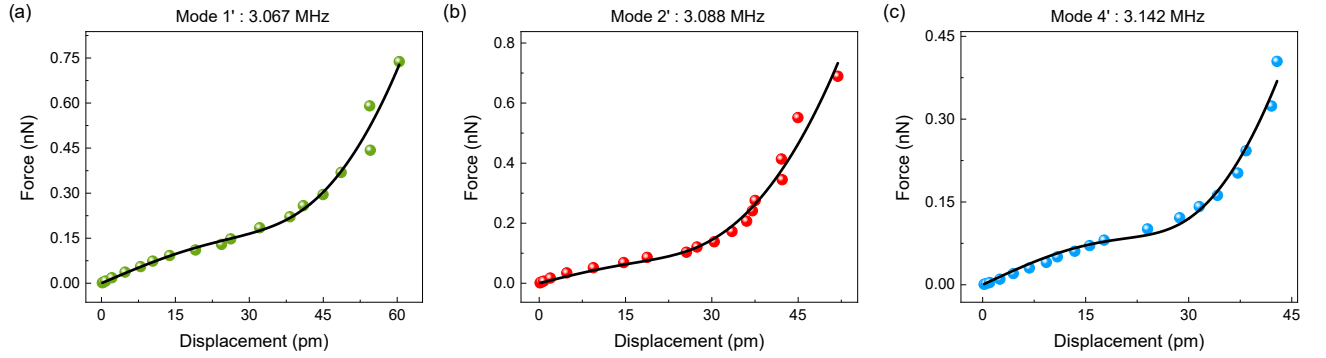


Figure S.6: **Nonlinear coefficient of hybrid SiNx modes: (a, b, c)** Force vs peak displacement plot of hybrid modes 1', 2' and 4' respectively, when coupled to graphene and probed on SiNx. SiNx modes experience a capacitive force due to ac gate voltage and a dominant backaction force from the graphene.

From fitting, for hybrid mode 1' we get  $C = 1.7(\pm 0.3) \times 10^{43} \text{ N/m}^3$ . The value of  $\beta_{hyb1}^s$  is calculated to be  $5.6(\pm 0.5) \times 10^{21} \text{ N/m}^3$ . Similarly for hybrid mode 2',  $\beta_{hyb2}^s = 8.0(\pm 0.8) \times 10^{21} \text{ N/m}^3$  and for hybrid mode 4',  $\beta_{hyb4}^s = 7.6(\pm 0.2) \times 10^{21} \text{ N/m}^3$  respectively. One can also estimate the nonlinear coefficient of the hybrid SiNx modes using critical displacement of that mode [3]. It is given by:

$$\beta_{hyb}^s = 1.54 \frac{m_s \omega_s^2}{Q_s x_c^2} \quad (\text{S.5})$$

For hybrid mode 1',  $x_c = 38.2 \text{ pm}$  and  $Q_s = 1316.5$  result in  $\beta_{hyb1}^s = 7.1(\pm 1.6) \times 10^{21} \text{ N/m}^3$ . Similarly for hybrid mode 2',  $\beta_{hyb2}^s = 7.6(\pm 1.5) \times 10^{21} \text{ N/m}^3$  and for hybrid mode 4',  $\beta_{hyb3}^s = 7.1(\pm 1.2) \times 10^{21} \text{ N/m}^3$ . It is remarkable to note that the hybrid modes of SiNx are well described by a Duffing-oscillator model and therefore, induced SiNx nonlinearities can be effectively described by Duffing constants for hybrid modes.

#### IV. Giant induced nonlinearity measured on SiNx surface

Here we provide few technical justifications for our usage of the term giant nonlinearity for Duffing constant as measured SiNx surface of graphene-SiNx hybrid modes. Our justifications is based on three estimates, all of which show orders of magnitude changes: (1) a comparison of nonlinear threshold of our hybrid modes to that of bare SiNx resonators without hybridization, as measured by different groups [4]. (ii) a comparison of average thermal displacement and threshold displacement ( $x^{cr}$ ) for the onset of nonlinearity for bare graphene, SiNx and hybrid SiNx modes show five orders of magnitude reduction of Duffing constant for hybrid modes. (iii) Following the work of D. Davidovikj *et. al.* [2], we use our estimated Duffing constant in to estimate corresponding effective Young's modulus of the bare or hybrid material. We find many orders of magnitude enhanced, effective Young's modulus, calculated this way. We further discuss the importance of having induced and tunable nonlinearity of the technologically important SiNx resonator modes.

##### A. Comparison of nonlinear threshold displacements for bare and hybrid SiNx resonators:

The threshold displacement corresponding to the bare SiNx ( $x_{bare}^{s,cr}$ ) is extracted using following relation:

$$x_{bare}^{s,cr} = x_{hyb}^{s,cr} \sqrt{\frac{\beta_{hyb}^s}{\beta_{bare}^s}} \quad (\text{S.6})$$

where  $\beta_{hyb}^s$  and  $\beta_{bare}^s (= 5 \times 10^{12} \text{ N/m}^3)$  denotes hybrid and bare (following ref. [4]) Duffing constant of SiNx. For mode 1,  $\beta_{hyb1}^s = 7.1 \times 10^{21} \text{ N/m}^3$  and  $x_{hyb1}^s = 38 \text{ pm}$  results in  $x_{bare}^{s,cr} = 1.2 \mu\text{m}$ . Similarly for mode 2,  $x_{bare}^{s,cr} = 1.4 \mu\text{m}$  and for mode 3,  $x_{bare}^{s,cr} = 1.2 \mu\text{m}$ . One can therefore note that such estimated displacement for onset of nonlinearity is 5 order of magnitude larger than that of hybrid SiNx.

##### B. Comparison of thermal displacement and displacement corresponding to nonlinear threshold:

The ratio of nonlinear threshold ( $x_{bare}^{g,cr}$ ) and thermal displacement ( $x_{th}^g$ ) for bare graphene is ( $4.6 \times 10^{-9}/1.04 \times 10^{-12} = 4.4 \times 10^3$ ). Using our parameters and expression of results ref. [4], in case of bare SiNx, the ratio are ( $1.4 \times 10^{-6}/24.5 \times 10^{-15} = 5.9 \times 10^7$ ), ( $1.2 \times 10^{-6}/23.7 \times 10^{-15} = 5.0 \times 10^7$ ) and ( $1.2 \times 10^{-6}/25.4 \times 10^{-15} = 4.7 \times 10^7$ ) for mode 1, 2 and 3 respectively.

However, for hybrid mode on graphene, ratio is ( $1.0 \times 10^{-9}/1.04 \times 10^{-12} = 1.0 \times 10^3$ ) and ( $1.2 \times 10^{-9}/1.04 \times 10^{-12} = 1.1 \times 10^3$ ), same order as that of bare graphene.

In case of SiNx hybrid modes the ratio drops by four orders of magnitude to ( $38.2 \times 10^{-12}/24.5 \times 10^{-15} = 1.6 \times 10^3$ ), ( $30.4 \times 10^{-12}/23.7 \times 10^{-15} = 1.3 \times 10^3$ ) and ( $31.5 \times 10^{-12}/25.4 \times 10^{-15} = 1.2 \times 10^3$ ).

##### C. Comparison of effective Young's modulus for bare and hybrid modes:

D. Davidovikj *et. al.* [2] suggest that effective Duffing constant can be used to estimate Young's modulus for the underlying resonator material. Using their relation [2],

$$E_i^g = \frac{(1.27 - 0.97\nu_g - 0.27\nu_g^2)R_g^2\beta_i^g}{\pi t_g} \quad (\text{S.7})$$

where  $E_i^g$  and  $\beta_i^g (i = bare, hyb)$  denotes Young's modulus and Duffing constant of bare and hybrid graphene respectively whereas  $\nu_g, R_g$  and  $t_g$  represents its Poisson ratio, radius and thickness respectively, we estimate Young's modulus for our measured Duffing constants. For bare graphene,  $\nu_g = 0.165$ ,  $R_g = 10 \mu\text{m}$ ,  $t_g = 0.34 \text{ nm}$  and  $\beta_{bare}^g = 5.8 \times 10^{13} \text{ N/m}^3$  results in  $E_{bare}^g = 6.0 \text{ TPa}$ , in agreement with prior measurements. For hybrid graphene mode, if we estimate such an effective Young's modulus, the value is,  $E_{hyb1}^g = 130 \text{ TPa}$  and  $E_{hyb2}^g = 89 \text{ TPa}$ , which is two order of magnitude larger than that of bare graphene.

The Young's modulus for square membrane [5] is given as:

$$E_i^s = \frac{(1 - \nu_s)a_s^2\beta_i^s}{21.90(1.45 - 0.43\nu_s)t_s} \quad (\text{S.8})$$

where  $E_i^s$  and  $\beta_i^s$  ( $i = \text{bare}, \text{hyb}$ ) denotes Young's modulus and Duffing constant of bare and hybrid SiNx respectively whereas  $\nu_s$ ,  $a_s$  and  $t_s$  represents its Poisson ratio, side length and thickness respectively. In case of hybrid SiNx mode 1',  $\nu_s = 0.24$ ,  $a_s = 320 \mu\text{m}$ ,  $t_s = 300 \text{ nm}$  and  $\beta_{\text{hyb}}^s = 5.6 \times 10^{21} \text{ N/m}^3$  leads to a giant value of  $E_{\text{hyb1}}^s = 4.9 \times 10^7 \text{ TPa}$ . Similarly for mode 2' and 4', we estimate effective Young's modulus to be  $7.0 \times 10^7 \text{ TPa}$  and  $6.7 \times 10^7 \text{ TPa}$  respectively. The estimated effective Young's modulus for the hybrid modes are eight orders of magnitude larger than that of bare SiNx ( $E_{\text{bare}}^s = 0.31 \text{ TPa}$ ).

#### D. Relevance of induced nonlinearity of SiNx modes:

SiNx resonators have shown significant promise towards quantum mechanics dominated dynamics for high-Q mechanical resonators at room-temperature. However, one needs to engineer nonlinearity in such a quantum device, to make it useful, Fluctuations of a classical resonator in thermal state is similar in shape in phase space to that of fluctuations of a harmonic oscillator dominated by zero point motion. For the resonator to be useful for precision measurement, one requires to squeeze the fluctuations in one quadrature, which requires nonlinear interactions. Similarly, for operations in quantum information devices, it is necessary to have condition switching and phase shifts, both of which requires nonlinear interactions of and between modes.

#### E. Relevance of tunable nonlinearity of SiNx modes:

While high-Q of SiNx resonators can result in resolving quantum fluctuations at room temperature, simultaneously storing a bit of information for a long time. On the other hand, as argued in the previous section, nonlinear response of graphene mode is necessary for inducing conditional logic or squeezed states. One would therefore like to tune effective nonlinearity in and out of resonance. Our device precisely allows to do this.

## V. Theoretical model

Here we discuss details of numerical simulations based on the model of coupled linear and non-linear oscillations of varying masses and quality factors. In this section, we analyse the model to provide evidence for the conjecture that the system is well described by hybrid modes, akin to that of normal modes for a corresponding linear system.

### A. Coupled linear SiNx and nonlinear graphene resonator

Our model is based on coupled modes of graphene and SiNx resonators, denoted by 1-dimensional amplitudes  $x_g$  and  $x_s$ , respectively and is described by the set of equations:

$$\ddot{x}_g = -\gamma_{\text{bare}}^g \dot{x}_g - \frac{\eta_{\text{bare}}^g}{m_g} x_g^2 \dot{x}_g - \frac{\beta_{\text{bare}}^g}{m_g} x_g^3 - [\omega_g^2 + \epsilon_p \cos(\omega_p t)] x_g + \frac{\alpha}{m_g} x_s \quad (\text{S.9})$$

$$\ddot{x}_s = -\gamma_{\text{bare}}^s \dot{x}_s - \omega_s^2 x_s + \frac{\alpha}{m_s} x_g \quad (\text{S.10})$$

where  $\gamma_{\text{bare}}^k$  and  $\omega_k$  ( $k = g, s$ ) represent linear damping and frequency of graphene and SiNx modes. Nonlinearity of graphene is quantified with two parameters: nonlinear damping  $\eta_{\text{bare}}^g$  and a cubic nonlinear response, characterized by its Duffing coefficient  $\beta_{\text{bare}}^g$ . The graphene mode is bilinearly coupled to a SiNx mode which is modelled by an effective interaction Hamiltonian,  $H_{\text{int}} = \alpha x_g x_s$ , where  $\alpha$  is a coupling constant. SiNx is considered to be a linear oscillator in the range of forcing that we apply in our experiments.

### B. Normal modes at low-amplitudes: probe on graphene and on SiNx resonators

At low external forcing, one can ignore nonlinear terms and thereby define two normal modes  $x_1$  and  $x_2$ . These modes extend over the entire device. However, we detect either on graphene ( $x_g$ ) or on SiNx ( $x_s$ ), which can be expressed as:

$$x_g = \frac{1}{2\sqrt{\alpha/m_s}} (x_2 + x_1) = x_2^g + x_1^g, \quad (\text{S.11})$$

and

$$x_s = \frac{1}{2\sqrt{\alpha/m_g}} (x_2 - x_1) = x_2^s - x_1^s \quad (\text{S.12})$$

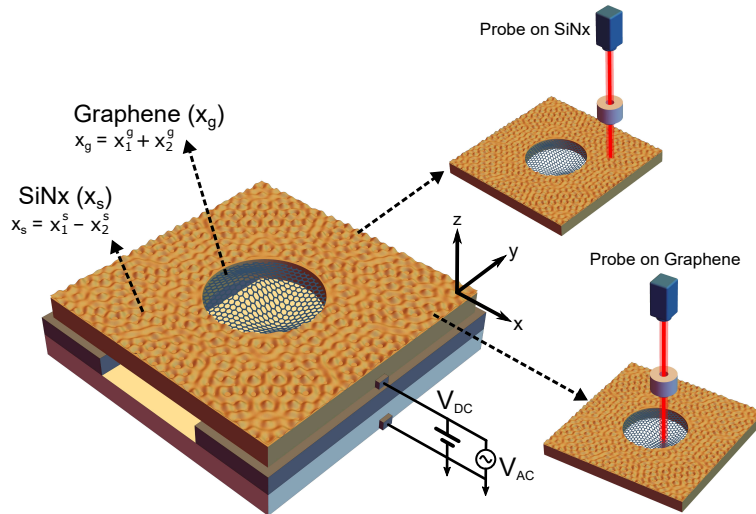


Figure S.7: **Experimental schematics:** Probing the two resonators graphene and SiNx, which according to eqn. S.8 and S.9 detects the motion of the coupled hybrid mode (i.e. mode 1 and mode 2).

The detected amplitudes of normal mode  $x_1$  (or  $x_2$ ) on graphene or SiNx are scaled by the ratio of square-root of respective masses ( $m_s/m_g \sim 10^4$ ). As a result, amplitude of normal mode 1(mode 2) on graphene i.e.  $x_1^g$  ( $x_2^g$ ) is two orders of magnitude larger than the amplitude of the same mode,  $x_1^s$  ( $x_2^s$ ), detected on SiNx surface. Accordingly, we have two Duffing constants for mode 1 (mode2):  $\beta_{\text{hyb1}}^g$  ( $\beta_{\text{hyb2}}^g$ ) detected on graphene and  $\beta_{\text{hyb1}}^s$  ( $\beta_{\text{hyb2}}^s$ ) detected on SiNx.

### C. Perturbative estimation I: Difference in $\beta_{\text{hybrid}}^{g/s}$ , measured on SiNx and graphene surfaces

The difference in scales of Duffing constants measured on SiNx and on graphene surfaces, can be understood in the following way: it can be noted that the nonlinear forcing ( $F_{NL}$ ) of a hybrid mode is uniform all along the spatial extent of the mode (later, in sec.V-E we argue for using effective normal mode models to understand steady state dynamics). However, since the hybrid mode for our device has physically two different kinds of oscillators with varying masses and surface areas, the force can be expressed as:  $F_{NL} = \beta_{\text{hyb}}^g x_g^3 = \beta_{\text{hyb}}^s x_s^3$ , as measured on graphene ( $x_g$ ) or on SiNx ( $x_s$ ). For a forcing  $F_0$  and assuming a steady state amplitude of  $x_{g,s} \sim F_0 Q_{g,s} / (m_{g,s} \omega_0^2)$  for graphene and SiNx, leads to an approximate ratio of the measured Duffing coefficients  $\beta_{\text{hyb}}^s / \beta_{\text{hyb}}^g \sim (m_s Q_g / m_g Q_s)^3 \sim 10^9$ . This is in accordance with our measured values of  $\beta_{\text{eff}}^{g,s}$  on graphene and on SiNx and provides a simple explanation of the giant nonlinearity measured on SiNx resonator surface.

### D. Perturbative estimation II: effective nonlinearity

To get an estimate of effective scaling of induced Duffing constant of SiNx hybrid mode,  $\beta_{\text{hyb}}^s$ , to that of graphene's mass ( $m_g$ ), bare Duffing constant,  $\beta_{\text{bare}}^g$  and coupling  $\alpha$ , perturbatively, let us consider the following simplified equations:

$$\ddot{x}_g + \omega_0^2 x_g + \beta_{\text{bare}}^g x_g^3 - \alpha_g x_s = 0, \quad (\text{S.13})$$

$$\ddot{x}_s + \omega_0 x_s - \alpha_s x_g = 0., \quad (\text{S.14})$$

where we have ignored damping and  $\alpha_i = \alpha/m_i$ , ( $i = g, s$ ).

For uncoupled graphene mode ( $\alpha_g = 0$ ) and assuming  $\beta_{\text{hyb}}^g x_g^3 \ll 1$ , standard perturbation methods yields a (zeroth-order) solution of the form:

$$x_g^{(0)} = A_g \cos \left[ \left( \omega_0 + \beta_{\text{bare}}^g \frac{3A_g^2}{8\omega_0} \right) t \right] - \frac{\beta_{\text{bare}}^g A_g^2}{32\omega_0^2} (\cos \omega_0 t - \cos 3\omega_0 t). \quad (\text{S.15})$$

where  $A_g$  is a constant set by initial conditions. Substituting this zeroth order expression of  $x_g^{(0)}$  in eqn. S.14, we arrive at

$$\ddot{x}_s + \omega_0 x_s - \beta_{\text{hyb}}^s x_s^3 = B \cos \omega_0 t, \quad (\text{S.16})$$

where, we have recognized  $\cos \omega_0 t$  as  $x_s^{(0)}/A_s$  ( $A_s$  being  $x_s^{(0)}$  when  $x_s$  and  $x_g$  are uncoupled) and defined:

$$B \equiv \alpha_s A_g - \frac{\alpha_s \beta_{\text{bare}}^g A_g^2}{8\omega_0^2}, \quad (\text{S.17})$$

$$\beta_{\text{hyb}}^s \equiv \frac{\alpha_s \beta_{\text{bare}}^g A_g^2}{8\omega_0^2 A_s^3}. \quad (\text{S.18})$$

Here, in the definition of  $B$ , we have ignored frequency correction.

We further note that the sign of  $\alpha_s$  determines whether the SiNx is effectively a soft or a hard nonlinear oscillator. From the expression of  $\beta_{\text{hyb}}^s$ , one can then express an effective scaling as:

$$\beta_{\text{hyb}}^s \propto \frac{\alpha_s \beta_{\text{hyb}}^g}{m_g^2}. \quad (\text{S.19})$$

### E. Perturbative estimation III: Modes at higher amplitudes

Experimental observations (fig.2b in main text) suggest strongly that there is a periodic solution for this system. So, averaging over the time period of oscillation, one can write  $\beta_{\text{bare}}^g x_g^3 = \beta_{\text{bare}}^g \langle x_g^2 \rangle x_g$ , and  $\eta_{\text{bare}}^g x_g^2 \dot{x}_g = \eta_{\text{bare}}^g \langle x_g^2 \rangle \dot{x}_g$  and at resonance,  $\omega_g = \omega_s$ . Using eqns. S.11 and S.12 in eqns. S.9 and S.10 we get

$$\begin{aligned} \ddot{x}_2 = \frac{1}{2} [ & -(\gamma_{\text{bare}}^g + \gamma_{\text{bare}}^s + \frac{\eta_{\text{bare}}^g}{m_g} \langle x_g^2 \rangle) \dot{x}_2 - (\gamma_{\text{bare}}^g - \gamma_{\text{bare}}^s + \frac{\eta_{\text{bare}}^g}{m_g} \langle x_g^2 \rangle) \dot{x}_1 - (2\omega_g^2 - 2\sqrt{\alpha^2/m_s m_g} \\ & + \frac{\beta_{\text{bare}}^g}{4m_g \alpha/m_s} \langle x_g^2 \rangle + \epsilon_p \cos(\omega_p t)) x_2 - (\frac{\beta_{\text{bare}}^g}{4m_g \alpha/m_s} \langle x_g^2 \rangle + \epsilon_p \cos(\omega_p t)) x_1 ], \end{aligned} \quad (\text{S.20})$$

$$\begin{aligned} \ddot{x}_1 = \frac{1}{2} [ & -(\gamma_{\text{bare}}^g + \gamma_{\text{bare}}^s + \frac{\eta_{\text{bare}}^g}{m_g} \langle x_g^2 \rangle) \dot{x}_1 - (\gamma_{\text{bare}}^g - \gamma_{\text{bare}}^s + \frac{\eta_{\text{bare}}^g}{m_g} \langle x_g^2 \rangle) \dot{x}_2 - (2\omega_g^2 + 2\sqrt{\alpha^2/m_s m_g} \\ & + \frac{\beta_{\text{bare}}^g}{4m_g \alpha/m_s} \langle x_g^2 \rangle + \epsilon_p \cos(\omega_p t)) x_1 - (\frac{\beta_{\text{bare}}^g}{4m_g \alpha/m_s} \langle x_g^2 \rangle + \epsilon_p \cos(\omega_p t)) x_2 ]. \end{aligned} \quad (\text{S.21})$$

Eqns. S.20 and S.21 can be written in compact form;

$$2\ddot{x}_{2,1} = -\Gamma \dot{x}_{2,1} - \gamma \dot{x}_{1,2} - (2\tilde{\omega}_{2,1}^2 + \epsilon_p \cos(\omega_p t)) x_{2,1} - (\frac{\beta_{\text{bare}}^g}{4m_g \alpha/m_s} \langle x_g^2 \rangle + \epsilon_p \cos(\omega_p t)) x_{1,2}, \quad (\text{S.22})$$

where  $\tilde{\omega}_{2,1}^2$ ,  $\Gamma$  and  $\gamma$  are defined as,

$$\tilde{\omega}_{2,1}^2 = (\omega_g^2 \mp \sqrt{\alpha^2/m_s m_g}) + \frac{\beta_{\text{bare}}^g}{8m_g \alpha/m_s} \langle x_g^2 \rangle, \quad (\text{S.23})$$

$$\Gamma = \gamma_{\text{bare}}^g + \gamma_{\text{bare}}^s + \frac{\eta_{\text{bare}}^g}{m_g} \langle x_g^2 \rangle, \quad (\text{S.24})$$

$$\gamma = \gamma_{\text{bare}}^g - \gamma_{\text{bare}}^s + \frac{\eta_{\text{bare}}^g}{m_g} \langle x_g^2 \rangle. \quad (\text{S.25})$$

For,  $\gamma_{\text{bare}}^g = \gamma_{\text{bare}}^s = \eta = 0$  (i.e.,  $\Gamma = \gamma = 0$ ;  $\beta = 0$  and  $\epsilon_p = 0$ ) eqn. S.22 reduces to

$$\ddot{x}_{2,1} = \omega_{2,1}^2 x_{2,1}, \quad (\text{S.26})$$

where,  $\omega_{2,1}^2 = \tilde{\omega}_{2,1}^2|_{\beta=0}$ .

The reduced eqn. S.26 suggests the ansatz,

$$x_{2,1}(t) = A_{2,1}(t) e^{-i\omega_{2,1} t}. \quad (\text{S.27})$$

Substituting eqn. S.27 in eqn. S.22 and ignoring  $\ddot{A}_{2,1}$  (rotating wave approximation) we get,

$$(\Gamma - 4i\omega_{2,1}) \dot{A}_{2,1} + \gamma e^{i\Delta t} \dot{A}_{1,2} = -(\epsilon_p \cos(\omega_p t) - i\omega_{2,1} \Gamma) A_{2,1} - (\epsilon_p \cos(\omega_p t) + \frac{\beta}{4\alpha/m_s} \langle x_g^2 \rangle - i\omega_{1,2} \gamma) A_{1,2} \quad (\text{S.28})$$

where,  $\Delta = \omega_1 - \omega_2$ .

For  $\Gamma = \gamma = \beta = 0$  equation S.28 becomes,

$$\dot{A}_{2,1} = -\frac{i\epsilon_p}{4\omega_{2,1}} \cos(\omega_p t) A_{2,1} - \frac{i\epsilon_p e^{\mp(i\Delta t)}}{4\omega_{2,1}} \cos(\omega_p t) A_{1,2}. \quad (\text{S.29})$$

We define,

$$A_{2,1}(t) = \tilde{a}_{2,1}(t)e^{\pm i\frac{(\omega_p - \Delta)}{2}t}. \quad (\text{S.30})$$

Plugging eqn. S.30 back in eqn. S.29 and dropping the terms with explicit phases like  $e^{\pm i\omega_p t}$  and  $e^{\pm 2i\omega_p t}$  we get,

$$\dot{\tilde{a}}_{2,1} = \mp \frac{i}{2}(\omega_p - \Delta)\tilde{a}_{2,1} - i\frac{\epsilon_p}{8\omega_{2,1}}\tilde{a}_{1,2}. \quad (\text{S.31})$$

Eqn. S.31 can be written in a matrix form,

$$\begin{bmatrix} \dot{\tilde{a}}_2 \\ \dot{\tilde{a}}_1 \end{bmatrix} = \begin{bmatrix} -\frac{i}{2}(\omega_p - \Delta) & -i\frac{\epsilon_p}{8\omega_2} \\ -i\frac{\epsilon_p}{8\omega_1} & \frac{i}{2}(\omega_p - \Delta) \end{bmatrix} \begin{bmatrix} \tilde{a}_2 \\ \tilde{a}_1 \end{bmatrix} \quad (\text{S.32})$$

with eigen values,

$$\lambda_{2,1} = \pm \frac{i}{2} \sqrt{(\omega_p - \Delta)^2 + \frac{\epsilon_p^2}{16\omega_2\omega_1}}. \quad (\text{S.33})$$

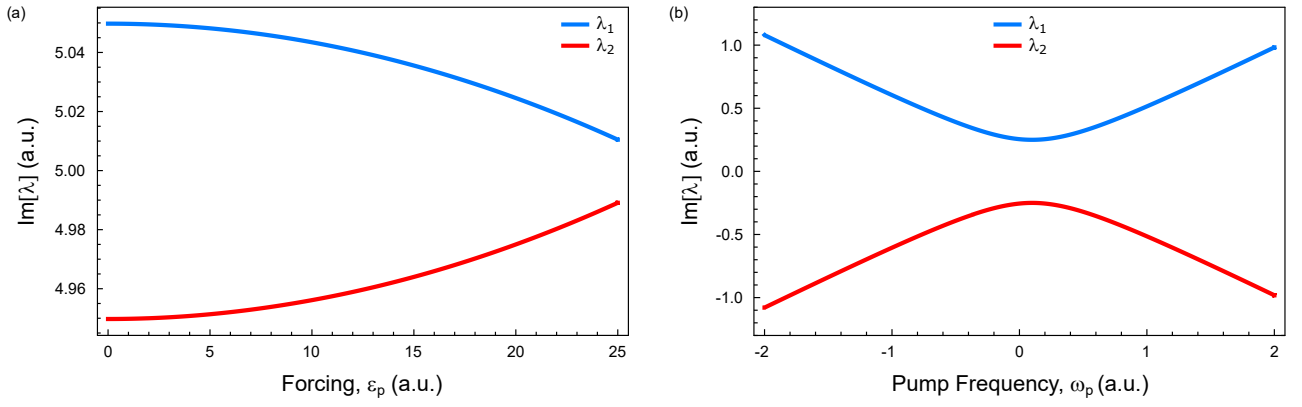


Figure S.8: **Eigen values**  $\lambda_{2,1}$ : Plotted as function of (a)Pump Amplitude( $\epsilon_p$ ) and (b)pump frequency( $\omega_p$ ).

The above simplified analytic estimation of effective normal modes provide insight into the nature of nonlinearity: that the insight of normal modes can be extended even in nonlinearity dominated self-oscillation regime. It explains experimental observation attraction of hybrid modes, with increasing forcing amplitude (fig. 2a,b) as an interplay of Duffing nonlinearity and nonlinear damping (fig. S8a). Similarly, the avoided level crossing of effective modes observed with pump detuning (fig. 3b,c) is well captured in a normal mode scenario (fig. S8b). Experimental evidence therefore seems to suggest that effective normal mode physic can be used to develop intuition of steady state dynamics (fig. 3a).

## VI. Frequency comb I: estimating nonlinear coefficients

The frequency comb spectra for estimating nonlinear coefficients from frequency comb spectrum in the instability regime. The parameters obtained from section II and from Table I were used to generate simulation spectra such as fig. 2c and fig. 3c in the maintext.

### A. Developing a methodology: Estimating nonlinear coefficient from simulated spectra

The parameters used in the numerical simulation of equations S.8 and S.9 were extracted by fitting the brownian spectrum (fig. S.2) of graphene with equation S.2. To reproduce fig. 2b (maintext), we carefully calibrate and match the spectra by toggling the free parameters i.e.  $\beta_{\text{bare}}^g$  and  $\eta_{\text{bare}}^g$ , as the brownian spectrum was considered to be devoid of nonlinear terms.

Table I: Parameters for numerical simulation

Parameter	unit	fig. 2c (pump voltage)	fig. 3c (pump detuning)
$m_g$	kg	$10 \times 6.25 \times 10^{-16}$	$10 \times 6.25 \times 10^{-16}$
$m_s$	kg	$2.38 \times 10^{-11}$	$2.38 \times 10^{-11}$
$\omega_g$	$s^{-1}$	$2\pi \times 2.864 \times 10^6$	$2\pi \times 3.005 \times 10^6$
$\omega_s$	$s^{-1}$	$2\pi \times 2.866 \times 10^6$	$2\pi \times 3.007 \times 10^6$
$\gamma_{\text{bare}}^g$	$s^{-1}$	$2\pi \times 25050$	$2\pi \times 8045.8$
$\gamma_{\text{bare}}^s$	$s^{-1}$	$2\pi \times 744$	$2\pi \times 496.4$
$\alpha$	$\text{kg s}^{-2}$	$4\pi^2 \times 2.328 \times 10^{-3}$	$4\pi^2 \times 3.4 \times 10^{-3}$
$\beta_{\text{bare}}^g$	$\text{N/m}^3$	$5.8 \times 10^{13}$	$1.07 \times 10^{12}$
$\eta_{\text{bare}}^g$	$\text{Ns/m}^3$	$9.8 \times 10^6$	$7.5 \times 10^4$

We observe that the asymmetry of the envelop enclosing the instability region increases when nonlinear coefficient ( $\beta_{\text{bare}}^g$ ) is increased (fig. S.9a) while the slope of the envelop curve changes with non-linear damping coefficient ( $\eta_{\text{bare}}^g$ ) (fig. S.9b).

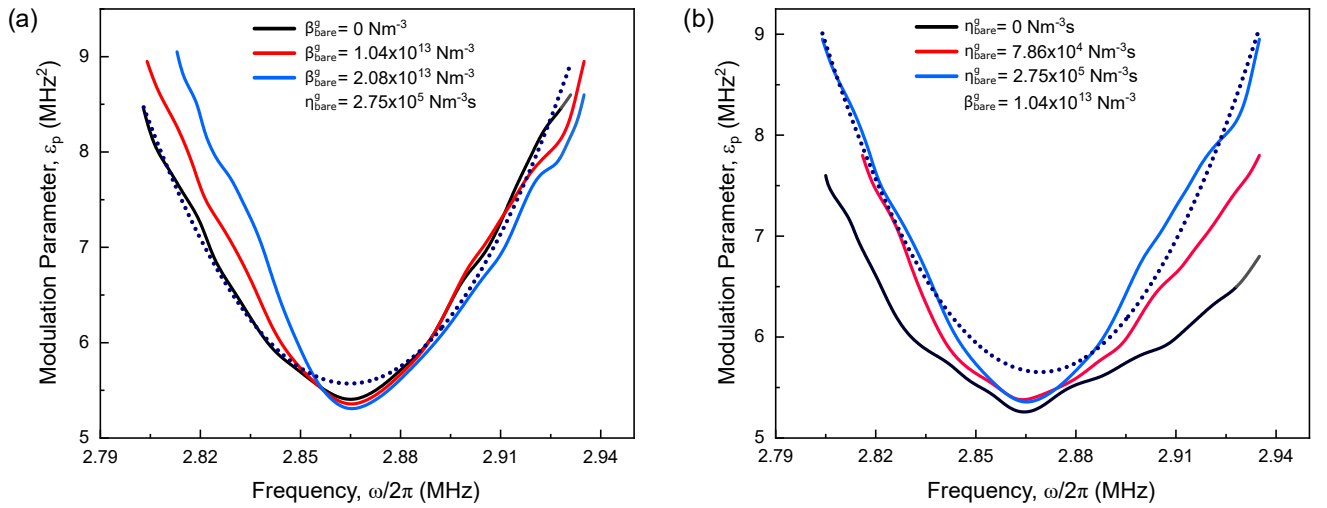


Figure S.9: **Interplay of  $\beta_{\text{bare}}^g$  and  $\eta_{\text{bare}}^g$** : The simulated profile of the instability region depends on the values of  $\beta_{\text{bare}}^g$  and  $\eta_{\text{bare}}^g$ , the curves illustrate the envelop of the instability region in accordance with fig. 3a in maintext. **(a)** For a fixed  $\eta_{\text{bare}}^g$  the asymmetry of the profile increases with increasing  $\beta_{\text{bare}}^g$  values. **(b)** For a fixed  $\beta_{\text{bare}}^g$  value, the simulated profile becomes narrower with increasing  $\eta_{\text{bare}}^g$  values.

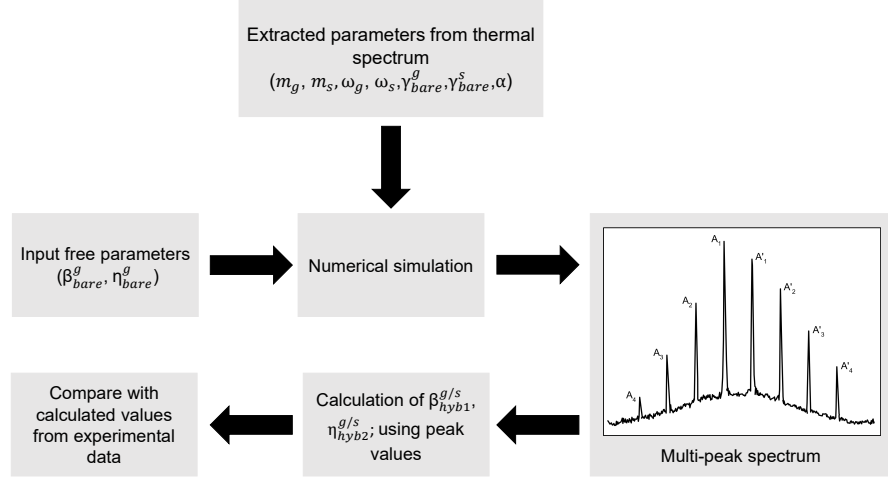


Figure S.10: A flow chart illustrating our method to estimate the nonlinear coefficients  $\beta_{\text{bare}}^g$  and  $\eta_{\text{bare}}^g$ .

### B. Methodolgy: Nonlinearity from comb amplitudes measured on any generic resonator surface

When hybrid mode is pumped at double of the resonance frequency, we observe parametric gain (fig. S.10b) in both the hybrid modes below the threshold of pump voltage. Above the threshold i.e. in the self-oscillation regime, we observe mode mixing which is attributed to the nonlinear terms in equation S.8,9. Using the amplitudes of newly generated modes, we calculate the nonlinear coefficients.

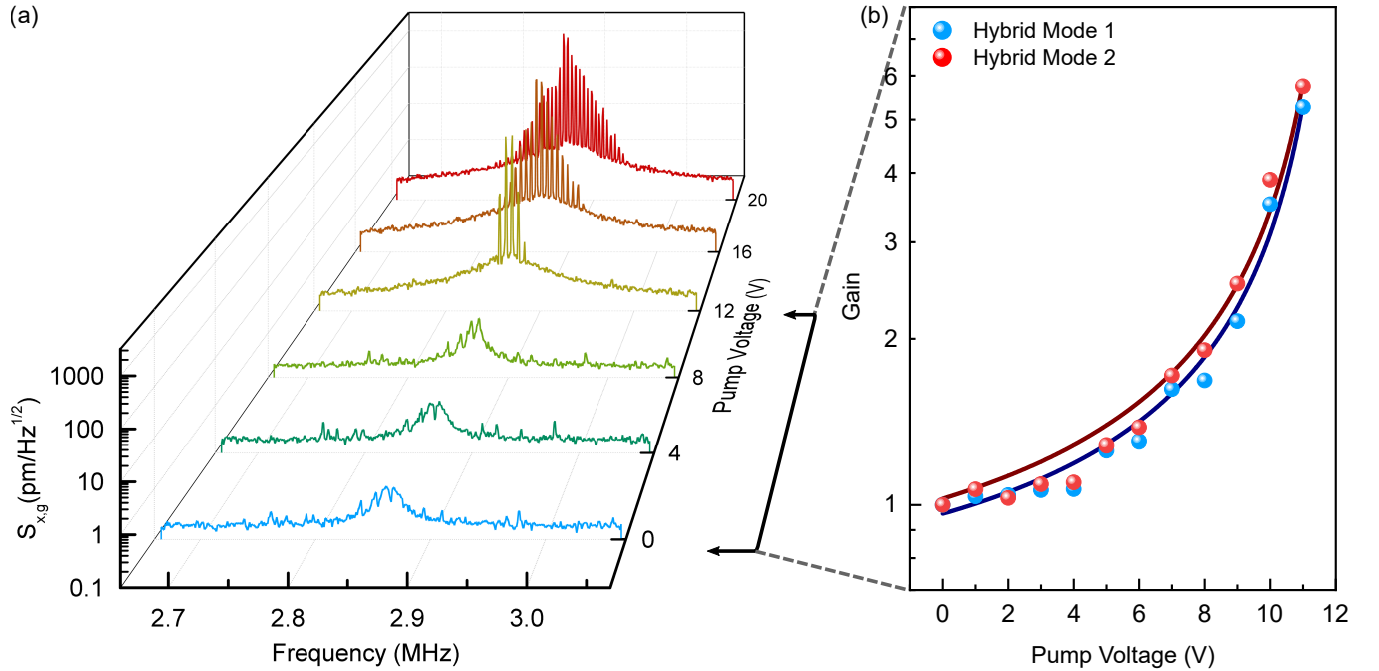


Figure S.11: **Multimode spectrum in graphene:**(a) Select cross-section plots of graphene-SiNx spectrum as a function of pump voltage from fig. 2b (maintext). (b) Plot of gain as a function of pump voltage for the two hybrid modes below the self-oscillation regime, the fitting curves were referred from ref. [1].

We start with the amplitudes of two hybrid modes to be  $a_1$  and  $a'_1$ , such that the corresponding displacement (measured on graphene or SiNx surface) can be expressed as:

$$x = (A_1 e^{-i\Delta t} + A'_1 e^{i\Delta t}) e^{i\omega_0 t} \quad (\text{S.34})$$

where,  $\Delta$  is the separation between modes from the central frequency,  $\omega_0$ . As evident from fig. 2(b) in maintext (or fig. S.11(a)), as we increase the pump voltage ( $V_p$ ) we have observe new modes which are equispaced by  $\Delta$ . So we go forward and write for four such modes the corresponding displacement (measured on graphene or SiNx surface) as:

$$x = (A_1 e^{-i\Delta t} + A'_1 e^{i\Delta t} + A_2 e^{-i3\Delta t} + A'_2 e^{i3\Delta t}) e^{i\omega t} \quad (\text{S.35})$$

where  $A_1$ ,  $A'_1$ ,  $A_2$  and  $A'_2$  are the amplitudes for the four hybrid modes at frequencies  $\omega_0 - \Delta$ ,  $\omega_0 + \Delta$ ,  $\omega_0 - 3\Delta$  and  $\omega_0 + 3\Delta$  respectively.

The observation of new generated modes are attributed to the terms with Duffing nonlinearity and nonlinear damping. Replacing  $x$  for the expressions of nonlinear damping and cubic nonlinear response terms, we get

$$\beta_{hyb}^k \langle x^2 \rangle x + \eta_{hyb}^k \langle x^2 \rangle \dot{x} = \beta_{hyb}^k (A_1 e^{-i\Delta t} + A'_1 e^{i\Delta t})^3 e^{i\omega t} + i\eta_{hyb}^k (A_1 e^{-i\Delta t} + A'_1 e^{i\Delta t})^2 \{(\omega - \Delta) A_1 e^{-i\Delta t} + (\omega + \Delta) A'_1 e^{i\Delta t}\} e^{i\omega t} \quad (\text{S.36})$$

where  $k = g, s$ .

In a frame rotating with a frequency  $\omega_0$ , the expression becomes:

$$\begin{aligned} \beta_{hyb}^k \langle x^2 \rangle x + \eta_{hyb}^k \langle x^2 \rangle \dot{x} = & \{e^{-3i\Delta t} (A_1^3 \beta_{hyb}^k + iA_1^3 (\omega - \Delta) \eta_{hyb}^k) + e^{-i\Delta t} (3A_1^2 a'_1 \beta_{hyb}^k + iA_1^2 A'_1 (\omega - \Delta) \eta_{hyb}^k) \\ & + e^{i\Delta t} (3A_1 A_1'^2 \beta_{hyb}^k + iA_1 A_1'^2 (\omega + \Delta) \eta_{hyb}^k) + e^{3i\Delta t} (A_1'^3 \beta_{hyb}^k + iA_1'^3 (\omega + \Delta) \eta_{hyb}^k)\}. \end{aligned} \quad (\text{S.37})$$

This leads to generation of new pair of frequency modes (first and last terms in above expression), whose amplitudes be  $a_2$  and  $a'_2$  such that they are separated from central frequency by  $\mp 3\Delta$  respectively. Further we plug eqn. S.32 in a forced simple harmonic oscillator equation and collect terms with same frequency. We observe that the amplitudes of new modes at  $\mp 3\Delta$  are related to their forcing as:

$$A_2 = \frac{F_2}{m[\{\omega_0^2 - (\omega_0 - 3\Delta)^2\}^2 + \{\gamma(\omega_0 - 3\Delta)\}^2]^{1/2}} \quad (\text{S.38})$$

and,

$$A'_2 = \frac{F'_2}{m[\{\omega_0^2 - (\omega_0 + 3\Delta)^2\}^2 + \{\gamma(\omega_0 + 3\Delta)\}^2]^{1/2}} \quad (\text{S.39})$$

Now comparing amplitudes  $a_2$  and  $a'_2$  from eqn. S.32-36 assuming  $\gamma$  to be small, we get

$$A_1^3 \beta_{hyb}^k + iA_1^3 (\omega - \Delta) \eta_{hyb}^k = 6A_2 \Delta \omega m_g \quad (\text{S.40})$$

and,

$$A_1'^3 \beta_{hyb}^k + iA_1'^3 (\omega + \Delta) \eta_{hyb}^k = 6A'_2 \Delta \omega m_g. \quad (\text{S.41})$$

The corresponding magnitudes are,

$$(\beta_{hyb}^k)^2 + (\omega - \Delta)^2 (\eta_{hyb}^k)^2 = 36 \left( \frac{A_2}{A_1^3} \right)^2 \Delta^2 \omega^2 m_g^2 \quad (\text{S.42})$$

$$(\beta_{hyb}^k)^2 + (\omega + \Delta)^2 (\eta_{hyb}^k)^2 = 36 \left( \frac{A'_2}{A_1'^3} \right)^2 \Delta^2 \omega^2 m_g^2 \quad (\text{S.43})$$

Similarly, to generate six modes i.e.  $x = (A_1 e^{-i\Delta t} + A'_1 e^{i\Delta t} + A_2 e^{-i3\Delta t} + A'_2 e^{i3\Delta t} + A_3 e^{-i5\Delta t} + A'_3 e^{i5\Delta t}) e^{i\omega t}$ , from four initial modes (eqn. S.34) and comparing the amplitudes  $A_3$  and  $A'_3$  we get,

$$9(\beta_{hyb}^k)^2 + (3\omega - 5\Delta)^2(\eta_{hyb}^k)^2 = 100 \left\{ \frac{A_3^2}{(A_1^2 A_2 + A_1' A_2^2)^2} \right\} \Delta^2 \omega^2 m_g^2 \quad (\text{S.44})$$

and

$$9(\beta_{hyb}^k)^2 + (3\omega + 5\Delta)^2(\eta_{hyb}^k)^2 = 100 \left\{ \frac{A_3'^2}{(A_1'^2 A_2' + A_1 A_2'^2)^2} \right\} \Delta^2 \omega^2 m_g^2 \quad (\text{S.45})$$

Solving equation S.41 and S.42 for the nonlinear coefficients, we finally get:

$$\beta_{hyb2}^k = \frac{\omega \Delta m_g}{\sqrt{12\omega\Delta}} \sqrt{100(\omega^2 - 2\omega\Delta) \frac{A_3^2}{(A_1^2 A_2 + A_1' A_2^2)^2} - 36(9\omega^2 - 30\omega\Delta) \left( \frac{A_2}{A_1^3} \right)^2} \quad (\text{S.46})$$

and

$$\eta_{hyb2}^k = \frac{\omega \Delta m_g}{\sqrt{12\omega\Delta}} \sqrt{-100 \frac{A_3^2}{(A_1^2 A_2 + A_1' A_2^2)^2} + 324 \left( \frac{A_2}{A_1^3} \right)^2} \quad (\text{S.47})$$

where  $\beta_{hyb2}^k$  and  $\eta_{hyb2}^k$  are nonlinear damping and Duffing nonlinear coefficient of the left ( $\omega_1$ ) hybrid mode. Similarly solving eqn. S.43 and S.44 for the right ( $\omega_2$ ) hybrid mode we get:

$$\beta_{hyb1}^k = \frac{\omega \Delta m_g}{\sqrt{12\omega\Delta}} \sqrt{-100(\omega^2 + 2\omega\Delta) \frac{A_3^2}{(A_1^2 A_2 + A_1' A_2^2)^2} + 36(9\omega^2 + 30\omega\Delta) \left( \frac{A_2}{A_1^3} \right)^2} \quad (\text{S.48})$$

and

$$\eta_{hyb1}^k = \frac{\omega \Delta m_g}{\sqrt{12\omega\Delta}} \sqrt{100 \frac{A_3^2}{(A_1^2 A_2 + A_1' A_2^2)^2} - 324 \left( \frac{A_2}{A_1^3} \right)^2} \quad (\text{S.49})$$

### C. Application I: Estimating nonlinear coefficients on graphene resonator surface

Based on the above methodology, estimated values of  $\beta_{hyb(2,1)}$  and  $\eta_{hyb(2,1)}$ , when probed on graphene, for fig. 2b (main text) are estimated and plotted with pump voltage in fig. S.12.

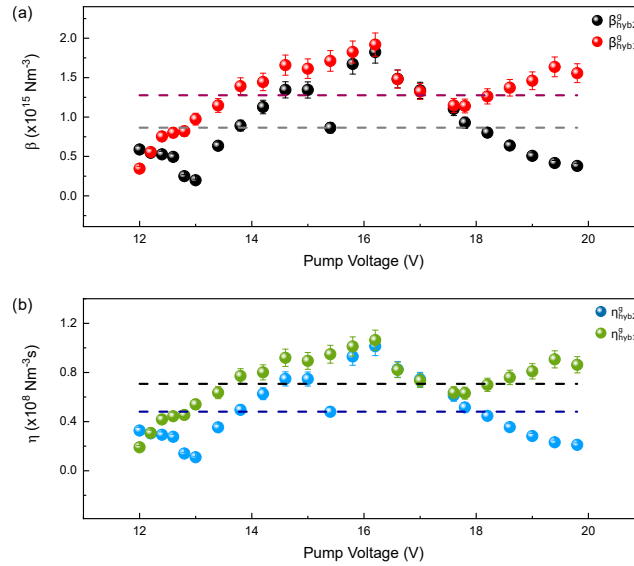


Figure S.12: **Estimated Nonlinear parameters from dataset:** Following our nonlinear coefficient estimation scheme we determine two values of  $\beta$  (a) and  $\eta$  (b) for the two branches of the instability region (see fig. 3a in maintext), assigned as  $\beta_{hyb(2,1)}$  and  $\eta_{hyb(2,1)}$  respectively, which have been plotted as a function of pump voltage. The dashed lines in the plots indicate the average value of the extracted parameters respectively.

The value of  $\beta_{2,1}$  and  $\eta_{2,1}$  for fig. 2c are calculated using the above scheme and are plotted with pump voltage in fig. S.13.

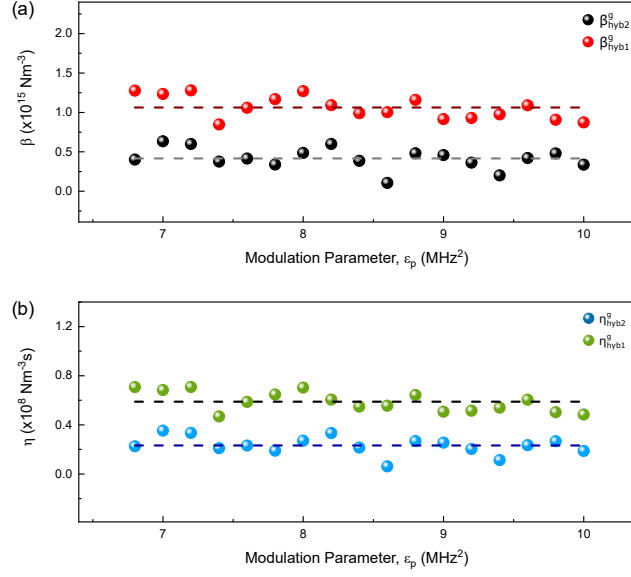


Figure S.13: **Estimated Nonlinear parameters from simulation:** We determine two values of  $\beta$  (a) and  $\eta$  (b) for the two branches of the instability region, assigned as  $\beta_{hyb(2,1)}$  and  $\eta_{hyb(2,1)}$  respectively. The values of nonlinear coefficients remain fairly constant with the pump voltage, unlike the ones estimated from experimental data. The dashed lines indicate the average value of calculated parameters respectively.

This method gives an estimate to the nonlinear coefficients of coupled hybrid graphene-SiNx mode from spectral measurements. The parameters might seem to have some dependence on pump voltage in fig S.12 but a definitive analysis is necessary to validate it. It will be pursued in a future work.

#### D. Application II: Estimating Duffing constant on Silicon Nitride resonator

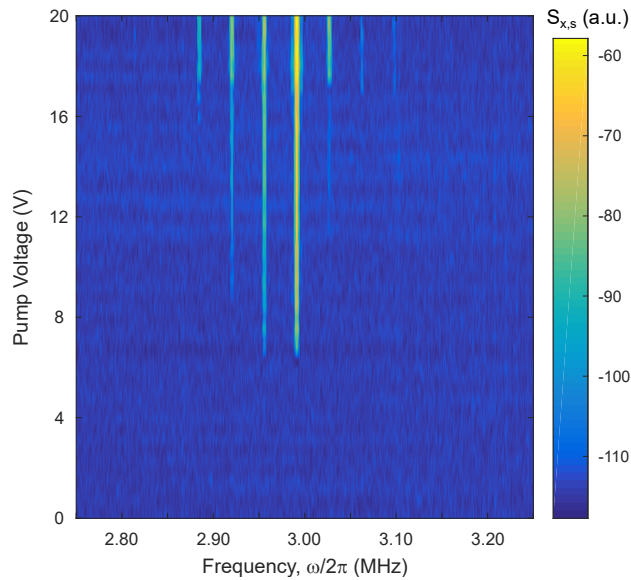


Figure S.14: **Experimental plot: Multi-mode spectrum on Silicon Nitride as a function of pump voltage.**

In the preceding sections we explored the system by directly driving the graphene modes, as well as directly driving the uncoupled and coupled SiNx modes. We also parametrically pumped the coupled graphene-SiNx hybrid modes and probed them on graphene. Now since it is a mode of the entire system, we expect similar observations when we probe on SiNx. But due to huge mass of Silicon Nitride resonator, the observations are mild versions of those when probed on graphene. Fig. 4 in the maintext and fig. S.14 below are results of when we parametrically pump the coupled hybrid mode and probe on SiNx. In particular fig. S.14 has a highly assymmetric envelop for the instability region.

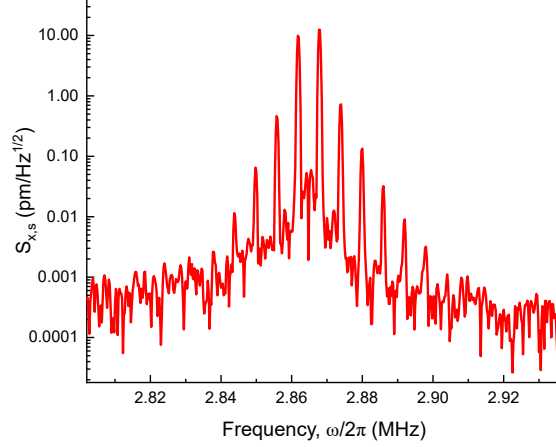


Figure S.15: **Simulation of induced multimode spectrum in SiNx with probe on SiNx.**

We simulate same, and observe multi-mode generation when we probe on SiNx, where its mode was taken to be linear,  $\beta_{bare}^s, \eta_{bare}^s = 0$ . Fig. S.13 shows the mixing behavior, further validating our observations. The nonlinear coefficients estimated from simulation plots (fig. S.15) using equation S.45-48 turns out to be,  $\beta_{hyb2}^s(\beta_{hyb1}^s) = 4.9 \times 10^{23} (4.7 \times 10^{23})$  N/m<sup>3</sup> and  $\eta_{hyb2}^s(\eta_{hyb1}^s) = 2.7 \times 10^{16} (2.6 \times 10^{16})$  Ns/m<sup>3</sup>.

## VII. Frequency comb II: Back-action force of graphene resonator mode on Silicon Nitride due to strong coupling

SiNx behaves as a linear resonator within its dynamic range for the maximum value of external forcing we can apply in our experiments i.e. its nonlinear coefficients are negligibly small and thus can be modeled under a force  $F_s$  as below:

$$\ddot{x}_s + \gamma_{bare}^s \dot{x}_s + \omega_s^2 x_s = \frac{F_s}{m_s} \quad (\text{S.50})$$

We bilinearly couple such a SiNx mode to a gate tunable graphene mode (a nonlinear oscillator) with coupling constant,  $\alpha$ . When at resonance, SiNx experiences additional force from graphene, a back-action force,  $F_{ba}(x_g) = \alpha x_g$  which only depends on graphene dynamic displacement. The modified equation for SiNx is written as:

$$\ddot{x}_s + \gamma_{bare}^s \dot{x}_s + \omega_s^2 x_s = \frac{F_s}{m_s} + \frac{F_{ba}(x_g)}{m_s} \quad (\text{S.51})$$

Using equation S.3 and S.4 and data points from fig. 1e, we are able to plot the capacitive forcing vs drive voltage in fig. S.16a. We repeat the same exercise but now we use the data points from fig. 1f and subtract the capacitive forcing contribution to generate fig. S.16b. We observe that the forcing due to back-action is approximately an order larger than the capacitive forcing.

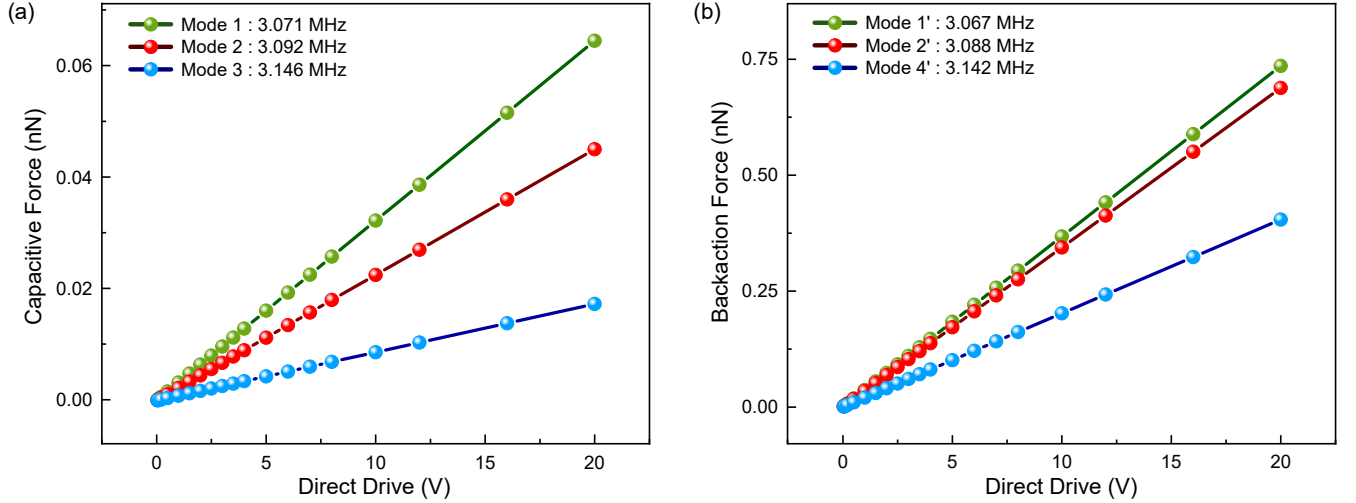


Figure S.16: **Backaction force on SiNx:** (a) Capacitive force acting on modes of SiNx as a function of drive voltage. (b) Backaction force experienced by SiNx modes coupled with graphene as a function of drive voltage.

## References

- \* Electronic address: gsaiakat@iitk.ac.in
- [1] Singh, R. *et. al* Motion Transduction with Thermo-mechanically Squeezed Graphene Resonator Modes. *Nano Lett.* **18(11)**, 6719 (2018).
  - [2] Davidovikj, D. *et.al* Nonlinear dynamic characterization of two-dimensional materials. *Nature Communications* **8**, 1253 (2017).
  - [3] Weber, P. *et.al* Coupling Graphene Mechanical Resonators to Superconducting Microwave Cavities. *Nano Letters* **14 (5)**, 28542860 (2014).
  - [4] Zwickl, B. M. *et.al* High quality mechanical and optical properties of commercial silicon nitride membranes *APL* **92**, 103125 (2008).
  - [5] Schomburg, W. K., 2011, Introduction to Microsystem Design, Springer, RWTH Aachen, Aachen, Germany.